



HAL
open science

Footprints and conditions of multistep alkali enrichment in basaltic melts at Piton de la Fournaise (La Réunion Island, Indian Ocean)

Guillaume Boudoire, Andrea Di Muro, Laurent Michon, N. Metrich

► **To cite this version:**

Guillaume Boudoire, Andrea Di Muro, Laurent Michon, N. Metrich. Footprints and conditions of multistep alkali enrichment in basaltic melts at Piton de la Fournaise (La Réunion Island, Indian Ocean). *Bulletin of Volcanology*, 2021, 83 (12), 10.1007/s00445-021-01508-6 . hal-03469106

HAL Id: hal-03469106

<https://hal.univ-reunion.fr/hal-03469106>

Submitted on 7 Dec 2021

HAL is a multi-disciplinary open access archive for the deposit and dissemination of scientific research documents, whether they are published or not. The documents may come from teaching and research institutions in France or abroad, or from public or private research centers.

L'archive ouverte pluridisciplinaire **HAL**, est destinée au dépôt et à la diffusion de documents scientifiques de niveau recherche, publiés ou non, émanant des établissements d'enseignement et de recherche français ou étrangers, des laboratoires publics ou privés.

Footprints and conditions of multistep alkali enrichment in basaltic melts at Piton de la Fournaise (La Réunion Island, Indian Ocean)

G. Boudoire^{1,2,3} · A. Di Muro^{4,5} · L. Michon^{4,6} · N. Metrich⁴

Abstract

Deciphering magma evolution below ocean basaltic volcanoes is all the more challenging because magma mixing is a common process tending to modify the pristine geochemical diversity during magma ascent. On the western flank of the Piton de la Fournaise volcano, transitional basalts have compositions that testify to origins down to the upper mantle and display a widespread geochemical diversity ranging from a tholeiitic affinity to an alkaline one. There, we show that evolved melt inclusions and matrix glasses ($\text{MgO} < 9 \text{ wt\%}$) record an alkali enrichment coupled with a Ca/Al ratio decrease, which tracks the effect of clinopyroxene crystallization at the depth of the mantle-crust underplating layer. At this depth and shallower, reverse zoning of olivine crystals, clinopyroxene dissolution, and hybrid melt compositions testify to extensive mixing processes leading to a homogenization of the pristine geochemical footprint of melts upon ascent. Enrichment in incompatible trace elements in some evolved melt inclusions suggests that magma ponding at the depth of the mantle-crust underplating layer favours also assimilation of melts originating from low degrees of partial melting of cumulates (wehrlites, dunites). Conversely, the most primitive melt inclusions documented so far at La Réunion Island (MgO up to 11.2 wt%) better preserve a pristine geochemical variability related to partial melting of a slightly heterogeneous mantle source. We suggest that these slightly distinct source components may mirror the compositions of recent melts from the two closely located Piton de la Fournaise and Piton des Neiges volcanoes.

Keywords Alkali enrichment · Basaltic melts · Ocean volcanoes

Introduction

Ocean basaltic islands are among the largest volcanoes on Earth. Their magmas commonly span large geochemical spectra (Dasgupta et al. 2010) predominantly mirroring pre-eruptive magma evolution in either deep (mantle) or shallow (crustal) reservoirs. Actually, magma ascent often proceeds by progressive steps of transfer between multiple magma ponding zones (Hildner et al. 2011; Klügel et al. 2015) that leads to the emission of variably degassed and apparently homogeneous evolved melts (Jennings et al. 2017). On the contrary, fast magma ascent in a few days/weeks from the deep part of the plumbing system up to the surface is less common, meanwhile favours the emission of gas-rich primitive melts at the surface, as at Kilauea (Hawaii; Helz et al. 2014; Poland et al. 2014; Rae et al. 2016).

At Piton de la Fournaise (PdF), historical eruptive activity, which mainly takes place inside the Enclos Fouqué caldera (central area), is characterized by weak intereruptive outgassing and by the emission of homogenous evolved and

✉ G. Boudoire
guillaume.boudoire@uca.fr

¹ Present Address: Laboratoire Magmas et Volcans, Université Clermont Auvergne, CNRS, IRD, OPGC, 6 avenue Blaise Pascal, 63178 Aubière, France

² GZG, Abt. Geochemie, Universität Göttingen, Goldschmidtstr. 1, 37077 Göttingen, Germany

³ Istituto Nazionale di Geofisica e Vulcanologia, Sezione di Palermo, Italy

⁴ Institut de physique du globe de Paris, CNRS, Université de Paris, F-75005 Paris, France

⁵ Observatoire volcanologique du Piton de la Fournaise, Institut de physique du globe de Paris, F-97418 La Plaine des Cafres, France

⁶ Laboratoire GéoSciences Réunion, Université de La Réunion, F-97744 Saint Denis, France

degassed transitional basalts. These “steady state basalts” have a chemical composition intermediate between tholeiitic and alkaline basalt and ascend from crustal reservoirs (Upton and Wadsworth 1966; Albarède et al. 1997; Boivin and Bachèlery 2009; Di Muro et al. 2014, 2015, 2016; Gurioli et al. 2018). Conversely, the NW rift zone (peripheral area, NWRZ), linking the Enclos Fouqué caldera with the quiescent neighbouring Piton des Neiges (PdN) volcano, has been recently found to be the locus of (i) a large emission of lavas with compositional and petrological variability (Valer 2016; Boudoire et al. 2019), (ii) significant soil CO₂ gas emissions (Liuzzo et al. 2015; Boudoire et al. 2017), and (iii) deep seismicity down to mantle level (Michon et al. 2015; Boudoire et al. 2017). The scoria cones within this rift zone emit transitional basalts with either a tholeiitic or an alkaline affinity, defined on the basis of the alkalinity index ($AI = [K_2O + Na_2O - 0.37 \times (SiO_2 - 39)]$; Rhodes 1996; Bureau et al. 1998a; Lénat et al. 2012; Walther et al. 2015; Valer 2016; Boudoire et al. 2019). As a whole, the geochemical variability of basalts emitted within the NWRZ has been mainly attributed to deep fractionation of clinopyroxene (Albarède et al. 1997; Brugier 2016; Boudoire et al. 2019), minor source effects (Valer et al. 2017; Boudoire et al. 2019), and contamination by small amounts of low-degree partial melts derived from cumulates (Boudoire et al. 2019).

However, the geochemical footprint of each process and the conditions favouring such melt variability remain still poorly constrained. Indeed, previous studies were mainly based on bulk rocks and experimental petrology that makes it challenging to decipher melt evolution during magma ascent. For instance, if the role of deep fractionation of clinopyroxene in the evolution of PdF melts has been extensively inferred (Albarède et al. 1997; Brugier 2016; Boudoire et al. 2019), barometric and physico-chemical conditions controlling clinopyroxene stability need further constraints. This is even more true considering that: (i) no clinopyroxene phenocrysts were described in basalts with an alkaline affinity, and (ii) the rare magnesian melt inclusions previously analysed do not present an alkali enrichment (Bureau et al. 1998a, 1999; Brugier 2016; Boudoire et al. 2019). Likewise, slight source effects were inferred by slight variations of some canonical incompatible trace element ratios (Nb/U; Valer et al. 2017) and Sr-Nd isotopes (Boudoire et al. 2019), but their origin and their influence on the full geochemical melt variability are not well established.

Here, we aim at identifying the geochemical characteristics of Piton de la Fournaise melts, determining the origin of their geochemical variability, and, more broadly, improving our understanding of magma evolution beneath ocean basaltic islands. To address these questions, we combined detailed geochemical study of melt inclusions and crystal zoning from a set of transitional basalts emitted along the NWRZ, whose bulk rocks have an alkaline affinity and show limited

crystal recycling. Our results are compared with those previously obtained from transitional basalts emitted in the same peripheral area and recording a tholeiitic affinity (Bureau et al. 1998b; Valer et al. 2017) and “steady state basalts” emitted in the central area since 1998 (Bureau et al. 1999; Vigouroux et al. 2009; Villemant et al. 2009; Di Muro et al. 2014). Our study fully complements previous works focused on the geochemical variability of lavas emitted at Piton de la Fournaise and aims at deciphering both the early steps of deep magma evolution and the footprints of magmatic processes controlling melt evolution in the plumbing system.

Geological settings

La Réunion Island (Indian Ocean) is the youngest intraplate basaltic island related to the hotspot that formed the Deccan flood province in India, 65 Myr ago (Mahoney et al. 2002). The 7-km-high volcanic edifice is built on the Indian oceanic crust with a Moho at 10.2–13 km below sea level (Gallart et al. 1999; Fontaine et al. 2015). Two volcanic edifices form the island (Fig. 1). Piton des Neiges (3.1 km asl) forms the north-western part of the island and is the oldest and largest edifice. Its subaerial activity started at least 2.2 Myr ago, and it has now been dormant for 29 kyr (Quidelleur et al. 2010; Salvany et al. 2012). Piton de la Fournaise (2.6 km asl) has been built on the south-eastern flank of Piton des Neiges starting at least 0.53 Myr ago. It is one of the most active basaltic shield volcanoes on Earth (Roult et al. 2012). Both volcanoes emit transitional magmas produced by partial melting of a common mantle source (Fisk et al. 1988; Hanyu et al. 2001; Valer et al. 2017). However, some authors have reported minor variations of incompatible trace and alkali elements (Fisk et al. 1988), and of Pb-Hf-Nd-Sr isotopes, which were attributed to either (i) the impingement of two small-scale blobs of plume material at the base of the lithosphere of La Réunion, one leading to the Piton des Neiges activity and the other to the Piton de la Fournaise activity (Bosch et al. 2008), or (ii) a two-step mixing involving three mantle source components (Nauret et al. 2019).

At Piton de la Fournaise, nearly 95 % of the eruptions since the eighteenth century took place inside the central Enclos Fouqué caldera, while less than 5% of the eruptions occurred along the rift zones radially cross-cutting the volcanic edifice (Fig. 1; Villeneuve and Bachèlery 2006; Michon et al. 2015). Central eruptions inside the Enclos Fouqué caldera and peripheral eruption along the NE and SE rift zones (NERZ and SERZ) are closely linked to the central shallow plumbing system and to the seawards displacement of the steep eastern flank (Michon et al. 2015; Peltier et al. 2015). This activity classically leads to the emission of strongly degassed transitional basalts displaying a very homogeneous evolved composition ($MgO = 6.5 \pm 0.8$

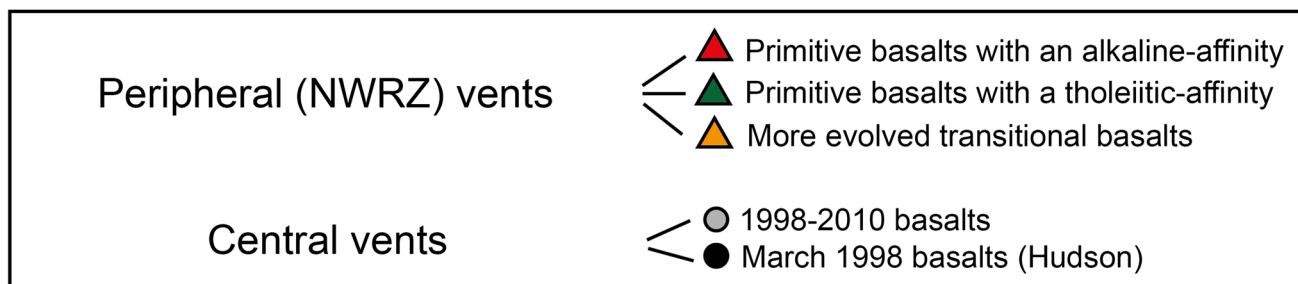
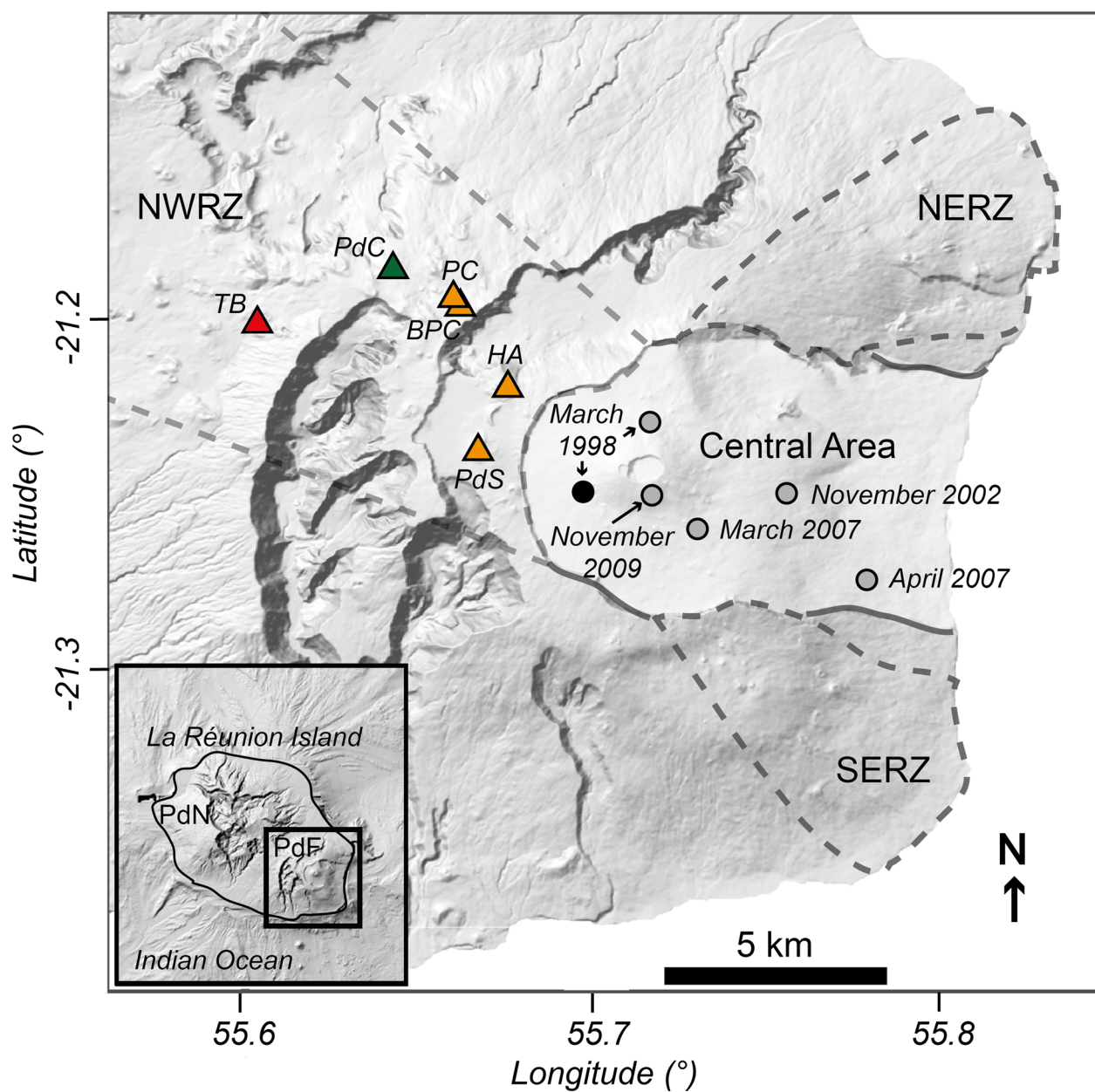


Fig. 1 Digital elevation model of the Piton de La Fournaise volcano, showing the main geomorphological features and the general trends of the three rift systems (dashed lines) converging towards the central area (Enclos Fouqué caldera): the North-West rift zone (NWRZ), the South-East rift zone (SERZ), and the North-East rift

zone (NERZ). The location of the eruptive products described in this study is reported (TB, Trous Blancs; PdC, Piton de Caille; PC, Petit Cratère; BPC, Below Petit Cratère; PdS, Plaine des Sables fall; HA, Piton Haüy). BPC refers to a lapilli layer close to the eruption of Petit Cratère

wt% and $K_2O+Na_2O = 3.5\pm 0.2$ wt% on average in glasses; Villemant et al. 2009; Di Muro et al. 2014, 2015, 2016). Conversely, the NW rift zone, on which we focus here, connects the western flank of Piton de la Fournaise with the older Piton des Neiges edifice. It has been proposed that the deepest part of the Piton de la Fournaise plumbing system is offset beneath the western flank of the volcano and that magma bodies settled beneath the NWRZ may feed the Piton de la Fournaise reservoirs and their eruptions (Michon et al. 2015; Liuzzo et al. 2015; Boudoire et al. 2017, 2019). The transitional basalts emitted within the NWRZ are generally more primitive and alkaline than the central ones ($MgO = 7.3\pm 0.8$ wt% and $K_2O+Na_2O = 4.0\pm 0.3$ wt% on average in glasses; Brugier 2016; Boudoire et al. 2019), show a bimodal distribution with tholeiitic and alkaline affinity (Brugier 2016; Valer et al. 2017), and are coeval with the central activity (Boudoire et al. 2019).

Sampling strategy

The few studies of basalts emitted along the NWRZ (peripheral area) of Piton de la Fournaise have been mostly based on (1) transitional lavas carrying an abundant amount of olivine crystals having a polymodal distribution (in size and composition) testifying to crystal recycling and accumulation (Bureau et al., 1998a, b; Welsch et al. 2013; Valer et al. 2017; Boudoire et al. 2019) and (2) aphyric transitional basalts with a tholeiitic affinity (Bureau et al., 1998a, b). In this study, we excluded lavas and pyroclasts carrying abundant and potentially recycled crystals in order to focus only on crystal-poor fast-quenched olivine basalts. Selected basalts were emitted by NWRZ vents extensively studied for the geochemistry of bulk rocks (Fig. 1; Walther et al. 2015; Valer 2016; Boudoire et al. 2019).

In order to cover the whole known geochemical diversity of basalts emitted from NWRZ vents, we selected basalts on the basis of their bulk rock Mg number ($Mg\# = [Mg^{2+} / (Mg^{2+} + Fe^{2+})]$) by assuming the proportion of Fe_2O_3 is 18% in Piton de la Fournaise melts, on average; Pichavant et al. 2016) and alkalinity index (AI; see equation above from Rhodes (1996)). These geochemical markers allow us to discriminate between primitive and more evolved basalts and transitional basalts with either an alkaline ($AI > 0$) or a tholeiitic affinity ($AI < 0$). We have selected fast-quenched unaltered pyroclasts (lapilli, scoriae, bombs) to minimize the effects of post-trapping processes that may have affected melt inclusions composition. Such an approach allows us to discriminate (Fig. 1; Table 1):

(1) Primitive basalts ($Mg\# > 0.65$) with either an alkaline ($AI = 0.4\pm 0.1$; Trouis Blancs: TB) or a tholeiitic affinity ($AI = -0.3$; Piton de Caille: PdC). Trouis Blancs (>9 kyrs) glassy lapilli layer is here investigated also for crystal

composition and zoning, fluid inclusions and melt inclusions composition, and barometry. Piton de Caille (<5 kyrs) basalts have been already analysed for crystal composition, fluid inclusions and melt inclusions composition, and barometry (Bureau et al. 1998b). We have completed here the PdC dataset with a study of crystal zoning.

(2) More evolved transitional basalts ($Mg\# = 0.60-0.62$; below Petit Cratère, BPC; Plaine des Sables fall, PdS; Piton Haüy, HA; Petit Cratère, PC) (Fig. 1). We studied the melt inclusions in all these products. Below Petit Cratère (<5 kyrs) glassy lapilli were also analysed for crystal composition and zoning, fluid inclusions composition, and barometry. A study of crystal zoning was also performed in basalts from Petit Cratère (470 yrs BP). Plaine des Sables (380 yrs BP) and Piton Haüy (<5 kyrs) glassy lapilli were previously analysed for crystal compositions and fluid inclusions (Boudoire et al. 2019), and we have completed the dataset with a study of melt inclusions composition.

Our analyses from basalts emitted from peripheral vents in the NWRZ were compared with published data on basalts from the 1998–2010 period emitted in the central area between two long periods of rest (1992–1998 and 2010–2014; Bureau et al. 1999; Vigouroux et al. 2009; Villemant et al. 2009; Di Muro et al. 2014). A particular attention was paid to basalts emitted at the Hudson central vent (H) during the 1998 central eruption, the only one characterized by a positive AI during this period and associated with deep seismicity and recording high pressures of crystallization down to the mantle depth (Bureau et al. 1999; Di Muro et al. 2016; Boudoire et al. 2019).

Lava and melt inclusions compositions are then correlated with the available bulk rock composition of intrusive rocks like dunites (D) and wehrlites (W) found as enclaves in tephra of La Plaine des Sables (Upton et al. 2000; Peters et al. 2016) and of gabbroic blocks (G) found scattered in the ashes of the Bellecombe explosive event (Upton et al. 2000), whose main characteristics are reported in Table 1.

Analytical methods

Mineralogy and crystal zoning

Zoning profiles in clinopyroxenes were acquired with a JEOL JXA-8900RL electron microprobe using 15 kV potential and 15 nA defocused beam coupled with a 5–15 s counting time per element (University of Göttingen, Germany). Relative errors are 0.5–1.5% (SiO_2 , MgO , FeO , CaO , Al_2O_3), 1–4% (TiO_2), 5–15% (Na_2O , Cr_2O_3 , NiO), and 5–35% (K_2O , MnO). Electron microprobe analyses on olivine were performed using a CAMECA SXFive at Camparis (Paris, France) with 15 kV, 20 nA focused beam, and a counting time varying from 10 to 50 s depending on the

Table 1 Main characteristics (eruption age, sample type, geochemical markers) of products studied in this research

Sites	Age (BP)	Sample type	Alkalinity index (AD)	CaO/Al ₂ O ₃	Mg#	⁸⁷ Sr/ ⁸⁶ Sr	Analysis (this study)	Analysis (literature)
<i>Peripheral eruptions: primitive transitional basalts</i>								
Trous Blancs: TB	> 9430	Lapilli	+0.4 ± 0.1 (n = 2)	0.74	0.65	0.704260 ± 0.000012	Melt inclusions-fluid inclusions-mineralogy-zoning	Bulk rock (Walther et al. 2015; Boudoire et al. 2019)
Piton de Caille: PdC	< 4175	<i>Free minerals in fallout bed</i>	-0.3 (n = 1)	0.79	0.72	0.704151	<i>Zoning</i>	Bulk rock (Valer 2016)-fluid inclusions/mineralogy/melt inclusions (Bureau et al. 1998a)
<i>Peripheral eruptions: more evolved transitional basalts</i>								
Below Petit Cratère: BPC *	< 4175	Lapilli	+0.1 ± 0.2 (n = 11)	0.77 ± 0.02	0.60 ± 0.02	-	Melt inclusions-fluid inclusions-mineralogy-zoning	-
Plaine des Sables fall: PdS	≈ 380 (last stage)	Lapilli	+0.9 ± 0.1 (n = 8)	0.68 ± 0.01	0.61 ± 0.01	0.704272	Melt inclusions	Bulk rock/fluid inclusions/mineralogy (Boudoire et al. 2019)
Piton Haüy: HA	< 4175 (early stage)	Lapilli	+0.9 (n = 1)	0.68	0.62	0.704291	Melt inclusions	Bulk rock/Fluid inclusions/Mineralogy (Boudoire et al. 2019)
Petit Cratère: PC	470	<i>Bomb</i>	-0.3 (n = 1)	0.76	0.60	0.704133	<i>Melt inclusions-zoning</i>	<i>Bulk rock/fluid inclusions/mineralogy</i> (Boudoire et al. 2019)
<i>Central eruptions: transitional basalts</i>								
1998-2010 “classical” eruptions: 98-10	1998-2010 AD	<i>Lava-lapilli</i>	-0.4 ± 0.2 (n = 146)	0.79 ± 0.02	0.62 ± 0.10	0.704162 ± 0.000022	-	<i>Melt inclusions</i> (Bureau et al. 1999; Vigouroux et al. 2009; Villemant et al. 2009; Di Muro et al. 2014)- <i>bulk rock/mineralogy</i> (Boudoire et al. 2019; <i>for a review</i>)- <i>fluid inclusions</i> (Famin et al. 2009; Boudoire et al. 2019)
March 1998 (Hudson): H	1998 AD	Lava-lapilli	+0.2 ± 0.1 (n = 7)	0.71 ± 0.01	0.61 ± 0.01	0.704248	-	Melt inclusions (Bureau et al. 1999; Valer et al. 2017)-mineralogy/fluid inclusions (Bureau et al. 1999)

Enclaves

Table 1 (continued)

Sites	Age (BP)	Sample type	Alkalinity index (AI)	CaO/Al ₂ O ₃	Mg#	⁸⁷ Si/ ⁸⁶ Sr	Analysis (this study)	Analysis (literature)
Dunite (Piton Chisny): D	-	Granular enclaves	+0.4 ± 0.2 (n = 30)	1.08 ± 0.62	0.86 ± 0.04	-	-	Bulk rocks (Upton et al. 2000; Peters et al. 2016)-fluid inclusions/mineralogy (Boudoire et al. 2019)
Wehrlite (Piton Chisny): W	-	Granular enclaves	-1.2 ± 0.9 (n = 3)	4.09 ± 0.26	0.86 ± 0.02	-	-	Bulk rocks (Upton et al. 2000; Peters et al. 2016)-fluid inclusions/mineralogy (Boudoire et al. 2019)
Gabbros (Bellevue): Bc): G	-	Granular enclaves	-0.7 ± 0.4 (n = 10)	1.15 ± 0.33	0.84 ± 0.03	-	-	Bulk rocks (Upton et al. 2000)

Fonts in regular are for basalts with an alkaline affinity and in italic for basalts with a tholeiitic affinity. Geochemical markers (alkalinity index = $K_2O + Na_2O - 0.37 \times (SiO_2 - 39)$, Mg#, CaO/Al₂O₃) were determined for bulk rocks (Valer 2016; Valer et al. 2017; Boudoire et al. 2019), except for BPC (*) for which only glassy groundmass has been analysed. The description of analyses performed in this study and sources of complementary published data are reported

element (Appendix 1). Relative analytical error measured is 0.8–4% for concentrations >15 wt%, 6–18% for concentrations in the 1–15 wt% range, and 15–100% for concentrations in the 1–0.2 wt% range. Absolute error on forsterite content (Fo) in olivine is <0.8 %.

Fluid inclusions and shrinkage bubbles

Fluid inclusions and shrinkage bubbles in melt inclusions were analysed at room temperature at IGP (Paris, France) using a Horiba T64000 Raman spectrometer manufactured by Jobin-Yvon, offering an excellent spectral resolution (<1 cm⁻¹) for peak identification (counting time: 2×180s). Fluid inclusions (Appendix 2) were excited using an argon ion laser at 488 nm wavelength with an average power of 1.13W. The stabilized laser power on the sample was not measured. Based on former acquisitions, we consider that it was in the range 10–100 mW and most probably lower than 100 mW because no surrounding glass was burnt during the analyses. Laser heating of fluid inclusions during analysis (>60 s per fluid inclusion) should lead to a constant and stable temperature increase in fluid inclusions in the range 4–100 °C above room temperature by considering the homogeneity of host crystal radius (around 1 mm), thickness (<400 μm), and mineralogy (olivine only in our case) (Hagiwara et al. 2021). In our study, the temperature of the fluid inclusions is estimated in the range 33–49 °C (during analyses) based on the relation linking the temperature to the intensity of CO₂ hot bands and of the Fermi dyad bands (Hagiwara et al. 2021; Appendix 2). Such a range of temperature allowed to exceed the critical temperature of CO₂ (31 °C) during the analysis. Consistently, no moving CO₂ vapour bubble was detected in fluid inclusions immediately after the analysis arguing for the presence of a homogenous CO₂ phase during the analysis. As reported by Boudoire et al. (2018) during the Raman investigation of CO₂-rich fluid inclusions in other samples from Piton de la Fournaise, no other gaseous species were detected in both fluid inclusions and shrinkage bubbles in melt inclusions over an extended spectral window of 200–4000 cm⁻¹.

Pressure estimates were obtained using the CO₂ density deduced from the Fermi dyad split (Δ ; van den Kerkhof and Olsen 1990; Frezzotti et al. 2012) between the 1388 and 1285 cm⁻¹ bands, using the equation of Wang et al. (2011) calibrated for Jobin-Yvon Horiba spectrometer at 1800-grooves/mm gratings with a 532-nm wavelength. This instrumental configuration is similar to that used in our study with the exception of the laser wavelength. However, laser wavelength plays only a minor role in the equations (maximum difference of 0.01 g.cm⁻³ for CO₂ density calculations with 514- and 532-nm wavelengths), whereas gratings and spectral resolution have a larger influence (up to 0.1 g.cm⁻³ between a 600- and a 1800-grooves/mm gratings) (Lamadrid et al. 2017). Raman spectra have been acquired on a single window collection according to the recommendations of Lamadrid et al. (2017).

The total uncertainty ($\epsilon(\text{TOT})$) on CO_2 density related to the use of the CO_2 densimeter of Wang et al. (2011) and to the analysis of fluid inclusions is:

$$\epsilon(\text{TOT}) = \sqrt{\epsilon(\text{analytical})^2 + \epsilon(\text{temperature})^2 + \epsilon(\text{processing})^2}$$

where $\epsilon(\text{analytical})$ is the uncertainty related to the use of the CO_2 densimeter of Wang et al. (2011), $\epsilon(\text{temperature})$ is the uncertainty related to the effect on the Fermi dyad of the heating of fluid inclusions by the laser (Hagiwara et al. 2021), and $\epsilon(\text{processing})$ is the uncertainty related to spectral resolution by peak fitting ($<0.014 \text{ g.cm}^{-3}$; Kobayashi et al. 2012). By comparing the CO_2 densimeters of Wang et al. (2011) with those obtained with an instrumental configuration close to that used in our study (Song et al. 2009; Fall et al. 2011; Lamadrid et al. 2017), the maximum difference between CO_2 densities ($\epsilon(\text{analytical})$) is 0.019 g.cm^{-3} for Δ in the range $103.7\text{--}104.45 \text{ cm}^{-1}$ (covering the range of fluid inclusions) and 0.031 g.cm^{-3} for Δ in the range $102.9\text{--}103.6 \text{ cm}^{-1}$ (covering the range of shrinkage bubbles). This analytical uncertainty overlaps also the standard deviation (0.011 g.cm^{-3}) on the equation of Wang et al. (2011). The temperature dependency of the Fermi dyad bands between 33 and $49 \text{ }^\circ\text{C}$ leads to a maximum $\epsilon(\text{temperature})$ of 0.018 g.cm^{-3} for Δ in the range $103.7\text{--}104.45 \text{ cm}^{-1}$ (covering the range of fluid inclusions) and 0.012 g.cm^{-3} for Δ in the range $102.9\text{--}103.6 \text{ cm}^{-1}$ (covering the range of shrinkage bubbles). Finally, $\epsilon(\text{TOT})$ in this study is equal to 0.029 g.cm^{-3} for fluid inclusions and 0.036 g.cm^{-3} for shrinkage bubble.

Rare sulphate and (hydrated) carbonates were sometimes detected in a few fluid inclusions. A similar observation was made by Boudoire et al. (2018, 2019) who highlight that the initial presence of a $\text{CO}_2\text{-H}_2\text{O}$ mixture has to be taken into account by considering $10 \text{ mol}\%$ of H_2O in the initial exsolved phase that leads to a density increase not exceeding 0.03 g.cm^{-3} (equation from Hansteen and Klügel (2008)). Corresponding pressures were estimated with the ISOC code provided by Bakker (2003) based on the equation of state (EOS) of Duan et al. (1992, 1996) for (i) $\text{CO}_2\text{-H}_2\text{O}$ mixtures ($90 \text{ mol}\%$ of CO_2 , $10 \text{ mol}\%$ of H_2O , and $0 \text{ mol}\%$ for the other species), (ii) fluid inclusions olivine(forsterite)-host, and (iii) a temperature of $1250 \text{ }^\circ\text{C}$ (intermediate temperature between that of melt inclusions and matrix glasses; Table 3). Any uncertainty on melt temperature results only in minor errors on pressure ($<50 \text{ MPa}$ for a shift of 100°C).

Melt inclusions and glasses

Major, trace, and volatile elements

Major elements in melt inclusions were measured with the CAMECA SX5 electron microprobe at Camparis (Paris, France) using 15 kV potential and 10 nA defocused beam

coupled with a counting time varying from 10 to 30 s depending on the element (Appendix 3). Analytical error measured is $<1.7\%$ for concentrations higher than $15 \text{ wt}\%$, $3\text{--}10\%$ for concentrations in the $2\text{--}15 \text{ wt}\%$ range, and more than 13% for concentrations $<2 \text{ wt}\%$. Measurements were reiterated when possible (between 2 and 7 measurements) in order to minimize the uncertainty (Appendix 3). Concentrations of volatiles in glasses (S, Cl, and P) were determined with a 30 nA defocused beam and a longer counting time (200 s) on peak (Appendix 3). Their accuracy was checked using international reference glasses (VG2: $\text{S}=1458 \text{ ppm}$ and $\text{Cl}=310 \text{ ppm}$; ALV98R23: $\text{S}=1110 \text{ ppm}$). Our measurements are $1423\pm 11 \text{ ppm}$ of S and $281\pm 12 \text{ ppm}$ of Cl for VG2 and $1076\pm 47 \text{ ppm}$ of S for ALV98R23. Detection limits are 46 ppm for S and 47 ppm for Cl.

Trace elements in melt inclusions, glassy matrices, and minerals were determined by laser ablation ((LA)-ICP-MS) using a 193 ArF excimer laser system (Resonetics M50) with a 7500 cs Agilent ICP-MS (LMV Clermont-Ferrand, France) with helium as carrier gas for analyses (Appendix 3). Laser repetition of $2\text{--}3 \text{ Hz}$ and a $26\text{--}44\text{-}\mu\text{m}$ diameter spot were used. The background was measured for 30s before ablation and acquisition. Calibration was made on a NIST 612 glass standard using CaO as the internal reference element. Reproducibility and accuracy are better than 10% for most elements with respect to the BCR2-G standard (Jenner and O'Neill 2012).

Dissolved H_2O

Dissolved H_2O in glasses was measured by Raman spectroscopy with a 514.5-nm wavelength argon ion laser using a Labram HR800 spectrometer (ENS Lyon, France) equipped with a Peltier-cooled CCD detector (Appendix 3). Analyses were performed by focusing a $1\text{-}\mu\text{m}$ -wide laser beam (average power on the sample of 7.4 mW) through an Olympus microscope in confocal setting with the highest magnification ($\times 100$). Spectra were collected in the $200\text{--}1500 \text{ cm}^{-1}$ (counting time of $2\times 30 \text{ s}$) and $2800\text{--}4000 \text{ cm}^{-1}$ (counting time of $2\times 50 \text{ s}$) domains corresponding to the aluminosilicate network + CO_2 domains and the $\text{OH}+\text{H}_2\text{O}$ domain, respectively. Selected analytical conditions minimize scatter from the embedding medium and prevent sample heating and oxidation. Calibration was performed on a set of basaltic reference glasses (H_2O_T Etna range: $0.4\text{--}3.04 \text{ wt}\%$; Mercier et al. 2009, 2010; Di Muro et al. 2014). Those glasses were regularly analysed during a same session in order to check and correct any potential instrumental drift. Water estimation was obtained by external calibration on peak intensities (H_2O_T band at 3580 cm^{-1}) and cross-checked with estimations from the internal calibration (silicate network band at 980 cm^{-1}) in order to correct potential errors related to defocusing (see Mercier et al. (2009) for a review of the

procedure). By reiterating analysis of the basaltic reference glasses, the accuracy of the analysis was better than 0.05 wt% H₂O, on average. In this study, reiteration of the measurements in a same melt inclusion led also to a standard deviation of 0.05 wt% H₂O on the average of the measurements that we consider as representative of the analytical uncertainty in this study.

Dissolved CO₂

Due to its low solubility in melts, quantifying the initial CO₂ in melt inclusions is challenging (Venugopal et al. 2020). Recent studies have highlighted the role of the shrinkage bubble in the underestimation of the CO₂ initially dissolved in the melt (Wallace et al. 2015; Aster et al. 2016; Tuohy et al. 2016; Venugopal et al. 2020) and promoted the combination of several analytical methods to recalculate it (Moore et al. 2015). In this study, we make an attempt to estimate the initial content of CO₂ dissolved in melt inclusion by adding the CO₂ exsolved in the shrinkage bubble ([CO₂]_{sh}) with that dissolved in the glass ([CO₂]_{glass}).

In the absence of carbonates in shrinkage bubbles (no peaks in the 1040–1100 cm⁻¹ Raman spectra; Frezzotti et al. 2012), the CO₂ content in shrinkage bubbles ([CO₂]_{sh}) was calculated using the formula of Hartley et al. (2014):

$$[\text{CO}_2]_{\text{sh}}(\text{ppm}) = 10^6 \times \frac{d_{\text{CO}_2} \times R_{\text{sh}}}{d_{\text{glass}} \times R_{\text{glass}}}$$

where d_{CO_2} is the CO₂ density (g.cm⁻³) of the shrinkage bubble estimated by the use of the Fermi dyad (see the methodology for fluid inclusions above) with an uncertainty of 0.036 g.cm⁻³ and d_{glass} is the glass wet density (g.cm⁻³) calculated from the equation of Lange and Carmichael (1987) based on the composition of melt inclusion (ranging from 2.63 to 2.72 g.cm⁻³ in this study). $R_{\text{sh}}/R_{\text{glass}}$ is the ratio between the volume of the shrinkage bubble and the glass, respectively. The petrographical estimation of this ratio assuming an ellipsoid and a sphere as representative of the melt inclusion and of the shrinkage bubble, respectively, may lead to a significant uncertainty due to the potentially irregular shape of melt inclusion ($\pm 10\%$; Hartley et al. 2014; Hanyu et al. 2020). To overcome this difficulty, we used the computational method of Riker (2005) that predicts the pre-eruption shrinkage bubble volume fraction as a function of the difference between trapping temperature and pre-eruption temperature. Both temperatures were estimated from the composition of the glass in the melt inclusion and of the embayment by using the thermometer of Helz and Thornber (1987), recalibrated by Putirka (2008). Predicted fraction of the shrinkage bubbles is lower than 1.9% in this study. Petrographical control performed on two melt inclusions has revealed that the absolute difference between

measured and estimated volume fraction of the shrinkage bubble is lower than 0.2% of the total volume in this study. This value is considered as representative of the uncertainty on volume fraction in this study. Only melt inclusion with a single shrinkage bubble and an apparent bubble volume fraction lower than 5% was investigated to avoid the analysis of pre-eruptive vapour bubbles trapped during crystal growth (Hanyu et al. 2020).

The residual CO₂ dissolved in the glass ([CO₂]_{glass}) was estimated by the use of the thermodynamically based model for the solubility of H₂O-CO₂ in silicate melt of Duan (2014) that is valid over a wide range of temperature, pressures, and melt compositions. Estimations of the residual dissolved CO₂ content with this model were performed by considering (i) the dissolved H₂O content determined by Raman spectroscopy and (ii) the pressure estimation from the CO₂ density of the shrinkage bubble (see details above). The variability on CO₂ content by taking into account the uncertainties on H₂O measurements and pressure estimation does not exceed 200 ppm of CO₂. Duan (2014) reports an additional uncertainty of 9.7% on the estimation of the CO₂ estimation in his model.

Results (with all the uncertainties described above) and details are provided in Table 3, together with some FTIR measurements performed in glassy melt inclusions.

Correction from post-entrapment processes

Melt inclusions were corrected for post-entrapment crystallization (PEC) on the basis of olivine-melt equilibrium ($K_D=0.306$; Fisk et al. 1988) and of clinopyroxene-melt equilibrium ($K_D=0.27$; Putirka 2008). These equilibrium values are in accordance with (i) recent and various experimental results obtained on Piton de la Fournaise melts (Brugier 2016) and (ii) conclusions from the modelling of predicted K_D as a function of the pressure, melt composition, and water content through the AlphaMELTS code (Boudoire 2017). At Piton de la Fournaise, Fe²⁺/Fe³⁺ in spinel ranges from 1.31 to 2.19 (1.83 in average). The correlation between forsterite content in olivine and the Fe²⁺/Fe³⁺ of hosted spinel (Bureau et al. 1998b; Boudoire 2017) was used to estimate the Fe²⁺/Fe³⁺ in basaltic melts (Maurel and Maurel 1982).

PEC values (see Appendix 3 for a full description) range from 0.1 to 5.8 % in melt inclusions from evolved peripheral basalts with an alkaline affinity (BPC, CHI, HA) to 6.3–12.4% in those from primitive peripheral basalts with an alkaline affinity (TB). A few primary melt inclusions trapped in clinopyroxene crystals from Trouis Blancs lavas and to a minor extent some primary melt inclusion in olivine crystals from La Plaine des Sables fall display a negative PEC percentage (down to -21%). These negative PEC percentages may reflect post-trapping dissolution of the walls of the host crystals (see Discussion). Melt inclusions from evolved peripheral basalts with a tholeiitic affinity (PC) undergo weak PEC

in olivine (2.6–7.2%) but record large PEC in clinopyroxenes (16.0–22.1 %). In order to select PEC threshold able to limit the influence of PEC on recalculated melt inclusions composition, we filtered melt inclusions based on the Mahalanobis distance method through a homemade Python code. This method allows recognizing outliers in multivariate datasets (De Maesschalck et al. 2000). A greater dispersion in major elements (CaO, SiO₂, MgO, FeO_T) contents (i.e. a higher frequency of outliers for each major element) is evidenced for PEC threshold >7.5 %, on average. For instance, Boudoire (2017) reports a greater variability of the FeO_T content in melt inclusions for PEC values >7.5 % ($2\sigma = 3.4$ wt%) than for PEC values <7.5 wt% ($2\sigma = 2.2$ wt%). Consequently, we retained only melt inclusions corrected from a PEC ranging from 0 to 7.5% (31 melt inclusions for 51 analyses performed) in order to minimize any bias related to the post-trapping processes.

Following the recommendations of Boudoire (2017) for the investigation of melt inclusions at Piton de la Fournaise, Fe loss correction (Danyushevsky et al. 2000; Gaetani and Watson 2002; Davis et al. 2003) was not applied in order to not introduce a bias due to the natural variability of FeO_T content in melt inclusion potentially linked to various extents of early clinopyroxene crystallization. Fe loss effect was only inferred for some melt inclusions in crystals from lavas erupted in the central area that are not the scope of this study. On the contrary, melt inclusions in crystals from tephra erupted in the peripheral area (like those investigated in this study) do not show evidence of Fe loss effect as testified by (i) the absence of systematic S loss related to the formation of sulphur globules (Danyushevsky et al. 2000), (ii) the absence of MgO enrichment, and (iii) the position of the melt inclusions close to the bulk rock-matrix glass line (see Boudoire (2017) for a complete discussion). As potential Fe loss is expected to significantly affect FeO_T and MgO content only (Tuohy et al. 2016; Boudoire 2017), this effect is even more limited in our study by excluding melt inclusions whose PEC is higher than 7.5% that have the largest variability in composition.

Results

Crystal zoning

Olivine

The composition of olivine phenocrysts in the primitive basalts with an alkaline affinity (TB) from NWRZ peripheral vents ranges from Fo_{80.1} to Fo_{87.7} (Fig. 2; Appendix 4). A main mode is identified at Fo_{86.5–87}, close to the equilibrium with the bulk rock (Fig. 2) and similar to that reported in primitive products with a tholeiitic affinity (PdC) from the same area (Fo_{85–87}; Bureau et al. 1998b).

In more evolved basalts (BPC) from the NWRZ, olivine composition is more iron-rich and ranges from Fo_{81.8} to Fo_{85.9}, with a main mode at Fo_{84.5–85} at the equilibrium with the hosting melt (Fig. 2; Appendix 4). This mode is consistent with that at the equilibrium with bulk rocks in other evolved basalts with an alkaline affinity (PdS, HA, PC; Fo_{83–85}) in the same area (Fig. 2; Boudoire et al. 2019).

In TB and PdC primitive basalts from the NWRZ area, the most magnesian olivine phenocrysts (i.e. Fo_{>85}) are unzoned (10 profiles; Fig. 3a, b). Only a few rare crystals with iron-rich cores were identified (Fo_{<84}). These inherited crystals show a progressive reverse zoning towards Fo_{85–85.5} rims (2 profiles; Fig. 3c).

In more evolved basalts from the NWRZ, the same pattern is observed: olivine crystals whose core composition is at the equilibrium with the hosting melt (Fo_{83–85} in BPC) are unzoned (3 profiles). Conversely, olivine crystals with iron-rich cores (Fo_{81–83}) are reversely zoned (4 profiles; Fig. 3d). For these inherited crystals, forsterite content is constant on the first 100–200 μm of the core and then progressively increases towards the rim (Fo_{84–85}).

In order to avoid the analysis of melt inclusions in inherited crystals retrieved during magma ascent, only unzoned homogeneously sized (>0.5 mm) olivine phenocrysts at the equilibrium with the hosting melt or even more magnesian were analysed for melt inclusions (Fig. 2).

Clinopyroxene

In the NWRZ area, clinopyroxene phenocrysts are abundant in primitive basalts with alkaline affinity (TB; Appendix 5). Their average composition (En₅₀Wo₄₀Fs₁₀) falls in the range of augitic composition previously reported in other peripheral clinopyroxene-bearing lavas (Appendix 5; Boudoire et al. 2019). Using a K_D = 0.27 for Fe-Mg partition between melt and clinopyroxene (Putirka 2008; Brugier 2016), we found that these clinopyroxenes are slightly more evolved (Mg# = 84) than expected from the composition of their host bulk rock (Mg# = 87).

In the more evolved basalts from NWRZ vents (PC; Appendix 5), augite phenocrysts have an average composition (En₄₉Wo₃₉Fs₁₂) similar to that analysed in primitive basalts with an alkaline affinity (TB). In these more evolved basalts, augite phenocrysts (Mg# = 0.85±0.02) are in equilibrium with the hosting bulk rock (Mg# = 0.85).

In primitive basalts from peripheral vents along the NWRZ (TB), the compositions of clinopyroxene cores and rims are indistinguishable. Conversely, clinopyroxene phenocrysts in more evolved basalts from NWRZ vents (PC) present both sector zoning in cores (crystal growth effect;

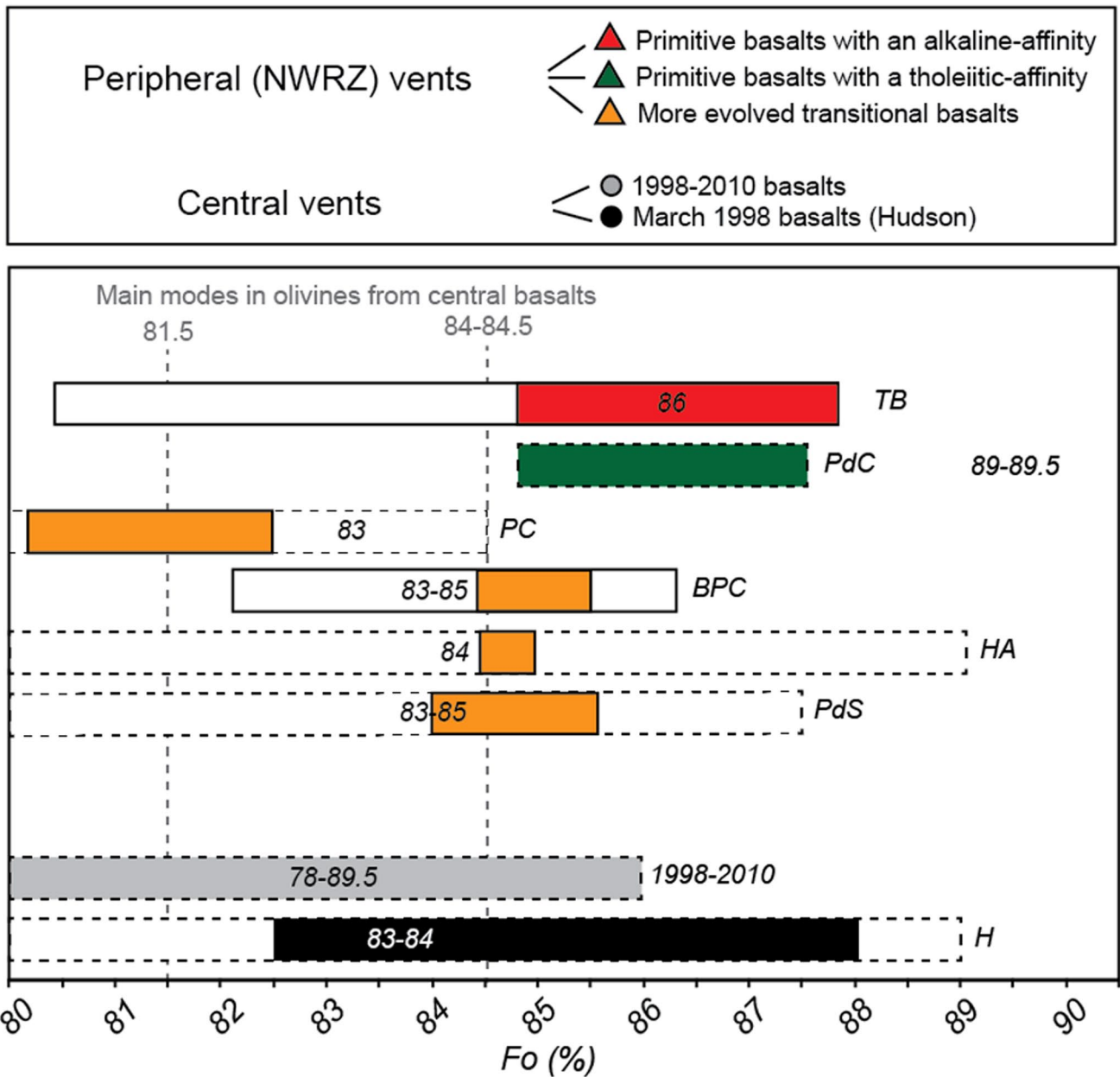


Fig. 2 Range of forsterite contents of olivine crystals in transitional basalts of Piton de la Fournaise. The analyses performed in this study are highlighted with continuous lines. Analyses from previous studies are highlighted with dashed lines (see Boudoire et al. (2019) for a

review). Numbers are the composition of olivine composition at the equilibrium with the hosting bulk rock. Filled coloured ranges are the composition of olivine crystals hosting melt inclusions described in this study

Kouchi et al. 1983; Mollo et al. 2010; Hammer et al. 2016) and oscillatory zoning in rims (Fig. 4; Fig. 5a, b). High-resolution (2–5 μm) elemental profiles from crystal core to rim (section cut across the c-axis; Fig. 5) reveal a progressive Mg depletion anticorrelated with Cr-Ti enrichment in cores, followed by various steps of Mg-Cr enrichment and Ti depletion towards the rims. The Mg-Cr-rich bands are often preceded by resorption surface (dark arrows on Fig. 5). Fe

contents and Ti/Al ratios are almost flat in most parts of the profiles (core and mantles) and increase close to the rim, independently of the oscillatory zoning (Fig. 5a).

Fluid inclusions

Measurements (46) of CO_2 fluid inclusions were performed in olivine phenocrysts from TB and BPC basalts to complete

the dataset available on basalts from peripheral vents along the NWRZ (Table 2; Bureau et al. 1998b; Boudoire et al. 2018, 2019). Even rare, isolated, and primary (Fig. 6a) CO₂ fluid inclusions are predominant in olivine phenocrysts of our samples. Secondary CO₂ fluid inclusions are only ubiquitous in rare olivine crystals not at the equilibrium with the hosting melt (Fig. 6b).

The density of the mixture CO₂+H₂O (90+10%) varies from 0.06 to 0.79 g.cm⁻³ without systematic difference between primary and secondary fluid inclusions. The corresponding pressures, which correspond to minimum trapping pressures (Hansteen and Klügel 2008), range between 3.3 and 4.4 kbar for fluid inclusions in olivine crystals from primitive basalt with an alkaline affinity (TB; Table 2). Interestingly, they overlap with the pressure domain reported from primitive basalts with tholeiitic affinity (3.1–5.7 kbar for PdC; Bureau et al. 1998b). The P_{CO₂+H₂O}, determined between 0.4 and 4.6 kbar for the more evolved BPC basalts, are in full agreement with those measured in other basalts with either a tholeiitic or an alkaline affinity emitted in the peripheral area along the NWRZ (Boudoire et al. 2019).

Melt inclusions

Melt inclusions (MIs) described in this study have been analysed far from cracks and do not present evidence of post-trapping crystallization as oxides and daughter minerals. Their longest axis varies from >200 µm to <50 µm independently of the hosting olivine composition. They present a well-rounded shape, are glassy, and often host a single shrinkage bubble (Fig. 6c). Because up to 80–90% CO₂ can diffuse into this bubble, the inferred initial CO₂ in melts can be highly underestimated (Moore et al. 2015; Aster et al. 2016). Hence, we tried to retrieve the CO₂ amount initially dissolved in the melt by measuring the P_{CO₂} into the bubble and the dissolved H₂O content (Table 3). The few melt inclusions hosting several bubbles and potentially trapping a deep exsolved fluid phase were not taken into consideration for the recalculation (Fig. 6c). Trail of fluid inclusions tracking volatile leakage from melt inclusions by decrepitation are sometimes present but rarely optically resolvable (Fig. 6d).

Major elements

The most magnesian melt inclusions (MgO = 10.8–11.2 wt%; CaO/Al₂O₃ = 0.82–0.83) described at Piton de la Fournaise are hosted in olivine Fo_{>85} of TB basalts (Fig. 7a; Table 4). Most of them (the inclusion Fo_{87.1} on Fig. 7b) have a positive alkalinity index (AI up to 0.7), which is correlated with high contents in alkali elements (K₂O + Na₂O = 3.4–3.7 wt%), in P₂O₅ (0.30–0.34 wt%), and in TiO₂ (2.5–2.8 wt%) and a low content in SiO₂ (<48 wt%; Fig. 7c).

A few melt inclusions (the inclusion Fo_{87.7} in Fig. 7b) have a tholeiitic affinity (AI down to -1.4), which is correlated with lower content in alkalis (K₂O + Na₂O = 3.0–3.1 wt%), in P₂O₅ (0.18–0.28 wt%), and in TiO₂ (2.4–2.5 wt%) and higher content in SiO₂ (49–51 wt%; Fig. 7c). The composition of this second group is fully comparable with that previously described in other high magnesian olivine crystals from lavas having a tholeiitic affinity (PdC: Bureau et al. 1998b; H: Bureau et al. 1999).

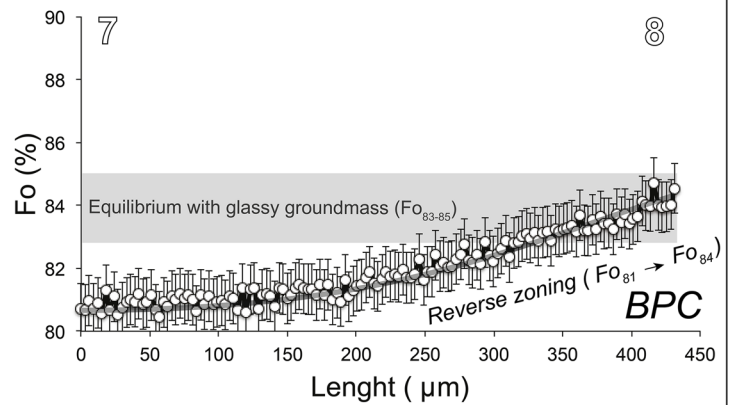
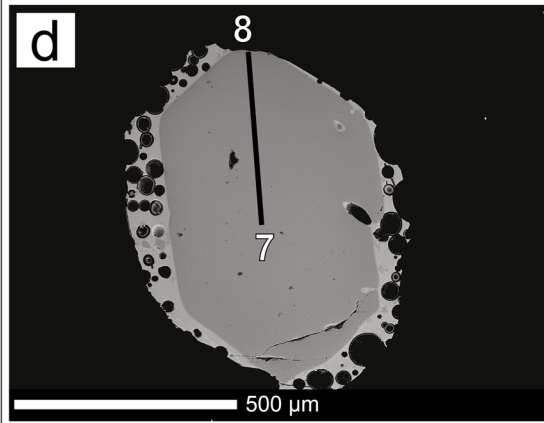
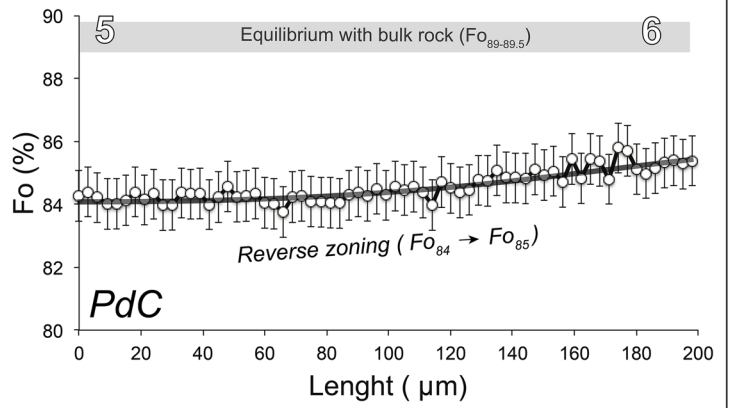
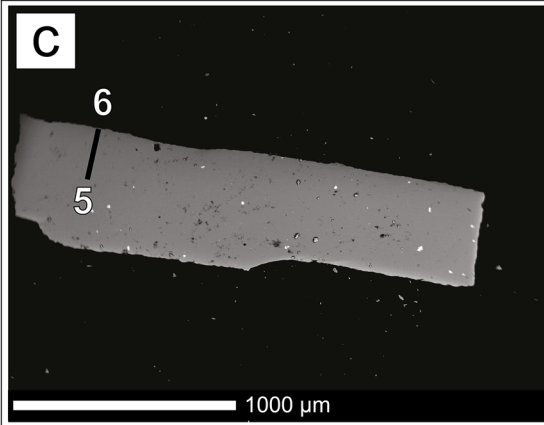
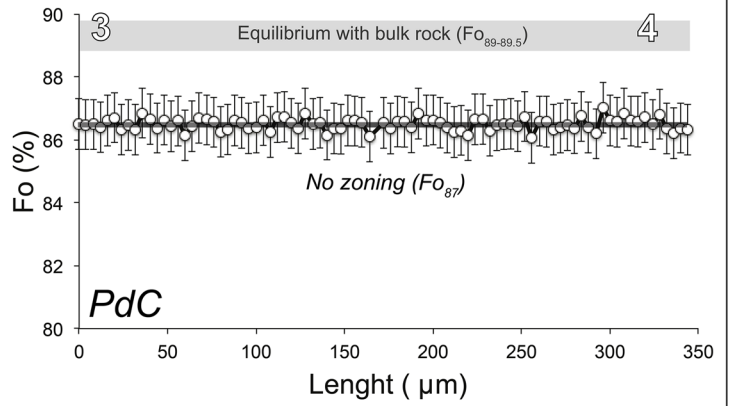
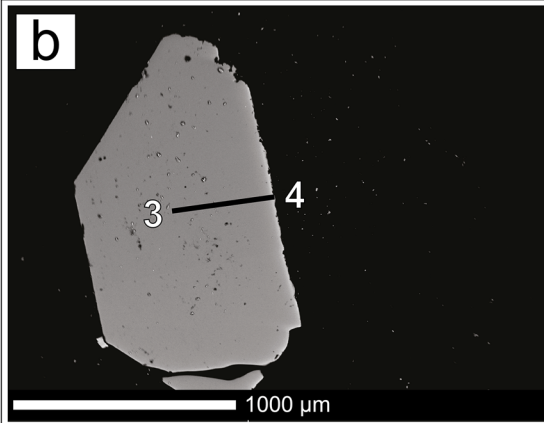
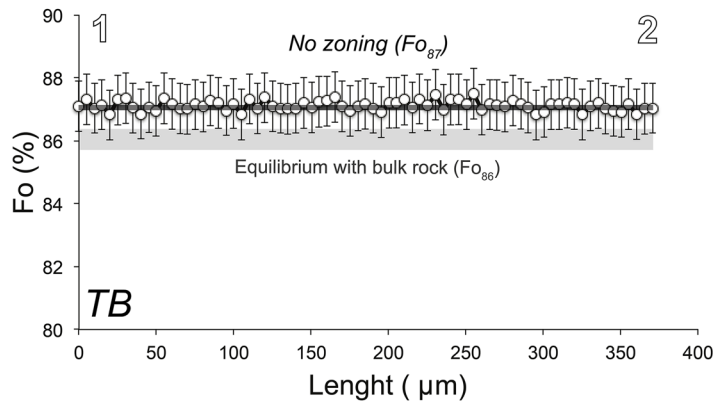
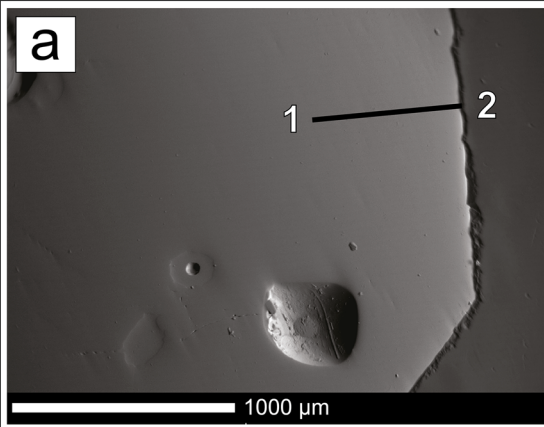
Melt inclusions in Fo_{<85} in BPC, PdS, and HA basalts display lower MgO contents (7.5–10.4 wt%) and CaO/Al₂O₃ ratio (0.71–0.87). Their contents in alkali elements (K₂O + Na₂O = 3.0–3.9 wt%), in P₂O₅ (0.26–0.40 wt%), in TiO₂ (2.3–3.0 wt%), and in SiO₂ (47–49 wt%) span the full range of compositions between the two poles observed in the most magnesian melt inclusions. Interestingly, similar variability is observed for melt inclusions previously analysed in olivine crystals from basalts emitted in the central area (Fig. 7).

In our dataset, the most evolved melts correspond to (1) melt inclusions in Fo_{<82} olivine crystals and En₄₇Wo₃₉Fs₁₄ clinopyroxene (MgO = 5.7–6.5 wt%; CaO/Al₂O₃ = 0.66–0.96) from PC basalts and (2) most of matrix glasses in all samples (MgO = 4.4–7.7 wt%; CaO/Al₂O₃ = 0.60–0.79).

Trace elements

The composition of high magnesian melt inclusions (TB) covers a relatively large range of compatible (Ni = 57–180 ppm; Co = 34–50 ppm; Fig. 8a, b, c), highly incompatible (Th = 1.4–2.5 ppm; La = 13–21 ppm; U = 0.39–0.60 ppm; Fig. 8d, f), and alkali (Ba = 94–202 ppm; Rb = 12–26 ppm; Fig. 8e) trace elements. Melt inclusions with a well-marked alkaline affinity (inclusion Fo_{87.1}, hereafter called “Pole 1”) are characterized by high contents in alkali (Ba, Rb) and highly incompatible (Th, La, U, Pb, Nb) trace elements (Appendix 3). Surprisingly, contents in highly compatible trace elements (Ni, Co, Sc) do not decrease (and in some cases increase) with the increasing contents in highly incompatible trace elements like Th (Fig. 8a, b, c).

The composition of more evolved melt inclusions (BPC, PdS, HA) covers an even larger range of trace elements contents that overlaps previous published data (Fig. 8; Di Muro et al. 2014; Valer 2016; Valer et al. 2017). Among more evolved melt inclusions, we address here the peculiar composition of two melt inclusions labeled Fo_{84.3} and Fo_{84.4} in Fig. 8. Together with the inclusion Fo_{87.1} (Pole 1) from TB, they mostly bracket the trace element geochemical diversity described in this study. The first one (inclusion Fo_{84.3}, hereafter called “Pole 2”) displays a similar content in compatible trace elements (Ni = 146 ppm; Co = 45 ppm) than Pole 1 (inclusion Fo_{87.1}) but is more depleted in both alkali (Ba = 94 ppm; Rb = 12 ppm) and incompatible (Th = 1.6 ppm;



◀**Fig. 3** Representative zoning profiles (Fo content) in olivine crystals from **a** Trous Blancs (TB), **b**, **c** Piton de Caille (PdC), and **d** below Petit Cratère (BPC) transitional basalts. The analytical uncertainty is reported for each point of the profiles

La = 15 ppm; U = 0.44 ppm) trace elements. The second one (inclusion Fo_{84.4}, hereafter called “Pole 3”) displays a similar content in highly incompatible trace elements (Th = 2.6 ppm; La = 22 ppm; U = 0.72 ppm) than Pole 1 but is more enriched in compatible trace elements (Ni = 353 ppm; Co = 59 ppm) and depleted in alkali trace elements (Ba = 140 ppm; Rb = 18 ppm).

As a matter of fact, the trace element composition of most melt inclusions lies between that of these three peculiar melt inclusions. For instance, ratios of variably incompatible trace elements such as La/Yb and Th/Yb mostly range between 8.6 ± 1.4 and 11.4 ± 1.9 and between 0.9 ± 0.1 and 1.4 ± 0.2 based on Pole 2 and Pole 1, respectively. Some ratios of highly incompatible trace elements (Ba/Th, Rb/Th, Nb/U, Ce/Pb) also show significant variations (Appendix 3). For instance, Ba/Th ranges between 53 ± 7 and 83 ± 13 in Pole 3 and Pole 1, respectively (Fig. 8e). On the contrary, other ratios, as La/Th and Th/U, do not show significant variations ($= 8.5 \pm 1$ and 3.6 ± 0.5 , respectively), with the exception of the matrix glasses, which are variably depleted in U independently on their composition in major elements (Fig. 7, Fig. 8f).

Volatiles

The composition of high magnesian melt inclusions (TB, PdC) covers also a relatively wide range of volatiles contents ($H_2O = 0.4\text{--}1.4$ wt%; $S = 585\text{--}3709$ ppm; $Cl = 210\text{--}418$ ppm). This range is similar to that previously defined by Bureau et al. (1998b) in melt inclusions in high magnesian olivine crystals from Hudson basalts (Fig. 9). Melt inclusions with a well-marked alkaline affinity (Pole 1) show high ratios of both highly and variably incompatible trace elements (Fig. 8) and also high Cl content ($Cl = 338$ ppm; Fig. 9a). On the opposite, those with a tholeiitic affinity (Pole 2 and PdC), having low ratios of highly and variably incompatible trace elements, display low Cl content ($Cl = 184$ ppm). Unfortunately, no data are available on dissolved volatiles and major elements for Pole 3, defined only on the basis of trace elements. However, melt inclusions with a composition in trace elements close to Pole 3 range intermediate between Pole 1 and Pole 2 in both Cl content and alkalinity. No noticeable systematic difference is observed regarding other volatiles such as H_2O (1.2 ± 0.2 wt%) and S (1797 ± 91 ppm) between these endmembers (Fig. 9b, c). A large variability of S (from 1706 to 585 ppm) and H_2O contents (from 1.4 to 0.4 wt%) can occur (TB) but without noticeable variations in K_2O (0.9–0.8 wt%) and FeO_T

(10.6–11.6 wt%) contents or PEC (4–6 %) and independently of the size of the melt inclusions.

The compositions of more evolved melt inclusions in olivine crystals from magmas emitted in both NWRZ (peripheral) and central areas broadly range between the compositions of the two endmembers Pole 1 and Pole 2 described above (Fig. 9a). An overall decrease in Cl, H_2O , and S contents is observed from evolved melt inclusions in olivine crystals from lavas from NWRZ vents ($Cl = 306 \pm 77$ ppm; $H_2O = 1.1 \pm 0.2$ wt%; $S = 1556 \pm 321$ ppm) to those from central vents ($Cl = 269 \pm 50$ ppm; $H_2O = 0.8 \pm 0.2$ wt%; $S = 1032 \pm 237$ ppm) and matrix glasses ($Cl = 237 \pm 29$ ppm; $H_2O = 0.2 \pm 0.1$ wt%; $S = 288 \pm 309$ ppm). We estimate that the extent of Cl degassing from matrix melts does not exceed 23% with respect to the pre-eruptive concentrations recorded by melt inclusions (black arrows on Fig. 9). Early sulphide saturation buffers the maximum pre-eruptive S concentration in the mafic melts from eccentric vents (Fig. 9c).

Dissolved CO_2 content in melt inclusions is highly variable for a same product (Table 3). For high magnesian melt inclusions (TB), recalculated CO_2 contents span a very large range from 13 ± 156 ppm to 3029 ± 564 ppm overlapping previous estimates made at Piton de la Fournaise without taking into account the CO_2 content trapped by the shrinkage bubble (PdC, 775–1765 ppm; Hudson, up to 4317 ppm; Bureau et al. 1998b, 1999). For more evolved melt inclusions, recalculated CO_2 contents also cover a large range from 283 ± 259 to 1518 ± 152 ppm.

Discussion

New insights on magma ponding and degassing at Piton de la Fournaise

Both pressures from CO_2 -rich fluid inclusions or recalculated CO_2 - H_2O saturation pressures in melt inclusions (Duan 2014) are undistinguishable between melts emitted along the NWRZ having either an alkaline or a tholeiitic affinity (Tables 2, 4).

The pressure distribution recorded by fluid inclusions brings the evidence of two main barometric modes and points out two levels of entrapment or reequilibration and multi-stage magma ascent (Figs. 10a, 11; Hansteen and Klügel 2008). The first and shallowest mode, at 0.3 kbar, is mostly recorded by fluid inclusions in olivine crystals from central lavas and highlights a well-constrained storage zone located close to sea level below the summit cone (Gallart et al. 1999; Peltier et al. 2009; Lénat et al. 2012; Di Muro et al. 2014; Fontaine et al. 2015; Lengliné et al. 2016). The second and main mode at 4.2 kbar is represented by the majority of fluid inclusions investigated in olivine crystals from eccentric magmas emitted along the NWRZ

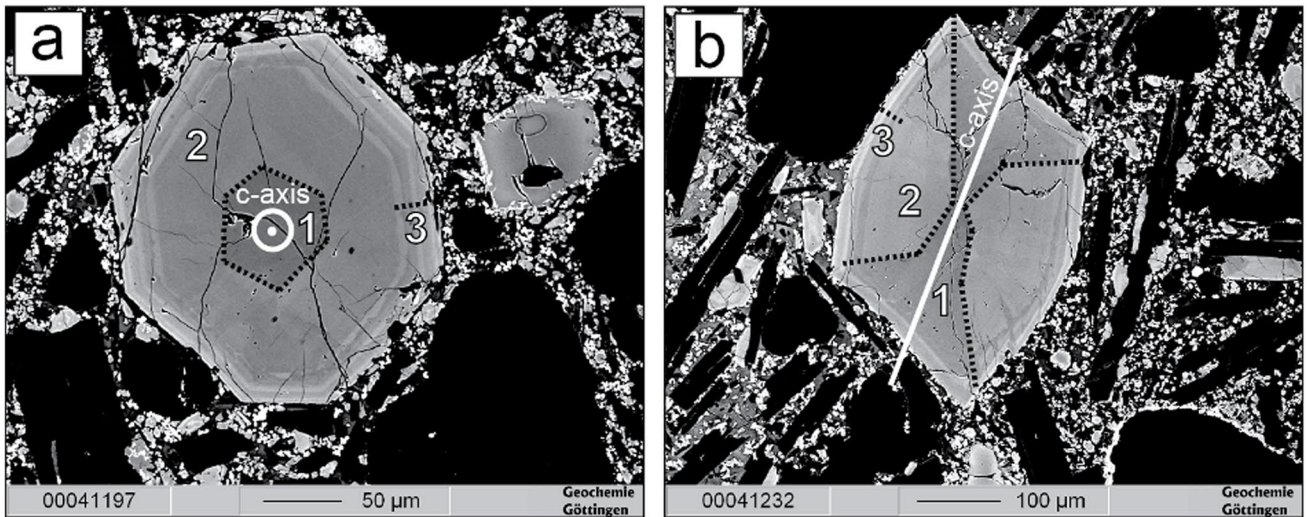


Fig. 4 BSE imagery of sector-zoned clinopyroxene in Petit Cratère (PC) bombs. **a** Section cut across the c-axis. **b** Section cut along the c-axis. 1, Mg-Si-rich and Ti-Al-Cr-poor core dark sectors. 2, Ti-Al-Cr-rich and Mg-Si-poor core bright sectors. 3, oscillatory zoning at the rims

and corresponds to the depth of the underplating layer at the mantle-crust transition (10–15 km below sea level; Figs. 10a, 11). A similar pressure mode was also identified by clinopyroxene barometry performed on lava samples erupted within the NWRZ (Boudoire et al. 2019). Higher pressures are rarely recorded by fluid inclusions (up to 5.7 kbar; PdC; Table 2) but testify to even deeper levels of crystallization located in the mantle (Figs. 10a, 11; Hansteen and Klügel 2008) as suggested by geophysical studies (Fontaine et al. 2015). The mantle-crust underplating layer is thus the main level recorded in the most magnesian olivine crystals cargo at Piton de la Fournaise and is the site of entrapment of a CO₂-rich fluid phase and of fluid inclusion reequilibration at high pressure.

We note that the average saturation pressure from melt inclusions is in most cases lower than that estimated from fluid inclusions in crystals from lavas emitted along the NWRZ (Fig. 10b; Table 4). The fluid inclusion barometry fully confirms that the CO₂-H₂O saturation pressures calculated on the basis of the dissolved contents of these two species are variably and potentially strongly underestimated, because of the diffusion of CO₂ into the shrinkage bubble (Fig. 6c; Wallace et al. 2015; Aster et al. 2016; Tuohy et al. 2016). A good agreement between fluid and melt inclusion barometry is observed in rare melt inclusions either hosted in magnesian olivine crystals from Hudson basalts (Bureau et al. 1999) or recalculated by taking into consideration the effect of the shrinkage bubble (our study). We found that the effect of the shrinkage bubble induces a pressure shift up to 3 kbar in our reconstructed melt inclusions as observed for some melt inclusions from Hudson olivine crystals (black arrow on Fig. 10b). Our results are consistent with previous findings of MacLennan (2017) who suggested that the

underestimation of the CO₂-H₂O saturation pressure in melt inclusions is generally <2.5 kbar and that less than 5% of melt inclusions are unaffected by this effect.

Our data on melt inclusions with an alkaline affinity provide a new opportunity to reconstruct magma evolution and degassing at Piton de la Fournaise starting from the mantle depth, below the NWRZ. We modelled the evolution of dissolved CO₂-H₂O in melts following both open- and closed-system degassing (1) assuming an initial content of dissolved CO₂ of 1.1 wt% in Piton de la Fournaise melts ponding at 10 kbar (Boudoire et al. 2018) and (2) starting from an initial dissolved water content of 1.4 wt% (Fig. 10b). This H₂O content corresponds to that measured in the most magnesian melt inclusions with an alkaline affinity (Pole 1; Table 4) and strikingly matches those with a tholeiitic one (1.3 wt%; Di Muro et al. 2014). Even if melt inclusions show a variable H₂O/K₂O ratio that cannot totally rule out the role of some source effects (as discussed further), the H₂O/K₂O variability mainly results from quite constant H₂O contents at variable K₂O contents (maximum of 1.3 and 1.4 wt% H₂O for high magnesian melt inclusions with a tholeiitic or an alkaline affinity, respectively). This behaviour mirrors a possible buffering of the H₂O content dissolved in melts ponding at the depth of the mantle-crust underplating layer, i.e. at the level of important reequilibration processes as suggested above (Boudoire et al. 2019).

Our data from recalculated CO₂-H₂O contents in melt inclusions with an alkaline affinity deviate from the modelled degassing trends because of higher CO₂/H₂O ratios. This behaviour is commonly reported in many basaltic volcanic systems (see Métrich and Wallace (2008) for a review) where high CO₂/H₂O ratios in melt inclusions, with respect to predicted degassing models, have been attributed to (1)

Fig. 5 Backscattered electrons (BSE) imagery of sector-zoned clinopyroxene in Petit Cratère (PC) bombs. Elemental profiles are reported with an analytical spacing varying between 5 μm (a) and 2 μm (b, c, d). The analytical uncertainty is reported for each point of the profiles. Only the most significant compositional changes are highlighted (filled coloured bars)

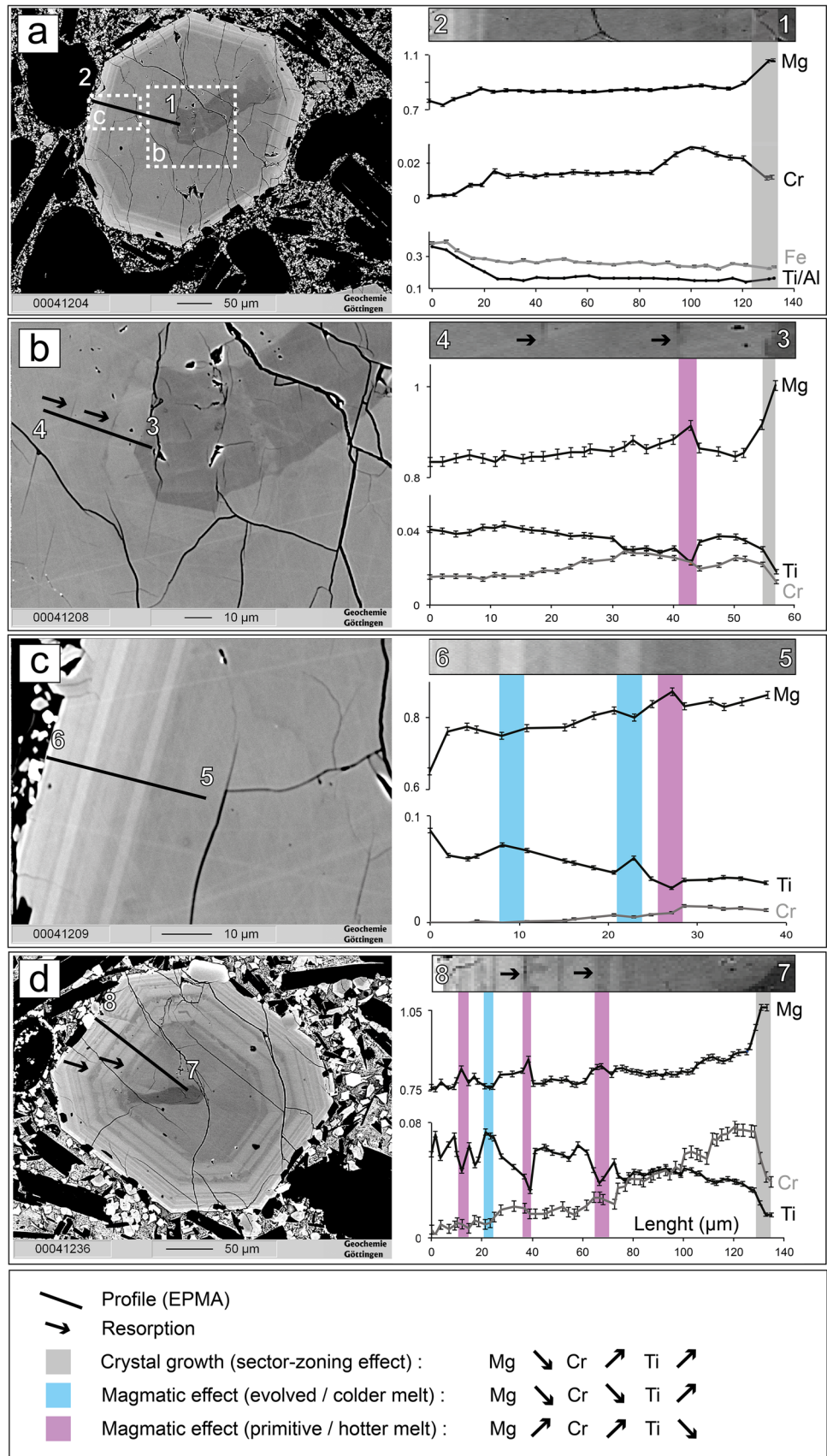
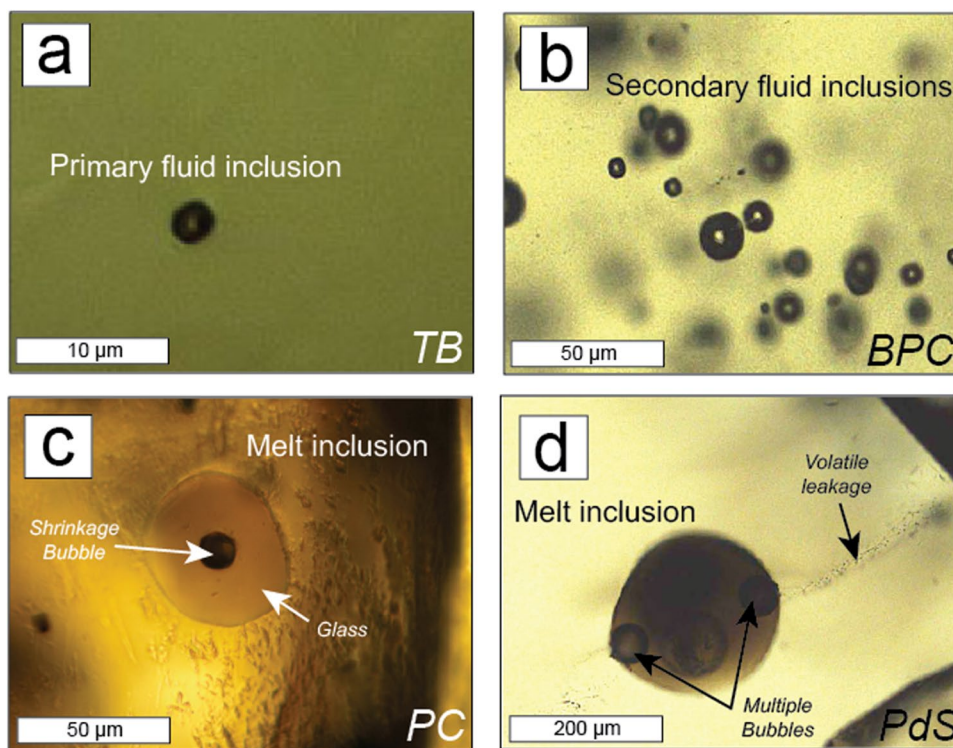


Table 2 Range of CO₂ densities and pressure calculation from fluid inclusions

		Number of analysis	FI density (g.cm ⁻³)		Pressure (kbar)	
			<i>d</i> _{min}	<i>d</i> _{max}	<i>P</i> _{min}	<i>P</i> _{max}
Peripheral eruptions: primitive transitional basalts	Trous Blancs (TB)*	5	0.66	0.77	3.3	4.4
	<i>Piton de Caille (PdC)</i>				3.1	5.7
Peripheral eruptions: more evolved transitional basalts	Below Petit Cratère (BPC)*	41	0.06	0.79	0.4	4.6
	Piton Chisny (CHI)				3.8	4.3
	Piton Haüy (HA)				4.2	4.7
	<i>Petit Cratère (PC)</i>				3.3	3.3
Central eruptions: transitional basalts	<i>Classical eruptions (98-10)</i>				0	0.9
	March 1998 (H)				3.5	

*for new data documented in this study. In italic, transitional basalts with a tholeiitic affinity. The uncertainty on the estimated pressures using the Fermi dyad (Raman spectroscopy) is lower to 0.4 kbar (see Methods)

Fig. 6 Transmitted light microphotographs of fluid and melt inclusions in olivine crystals from basalts emitted along the NWRZ. **a** Primary fluid inclusion in an olivine crystal from Trous Blancs basalts (TB). **b** Trail of secondary fluid inclusions in an olivine crystal from below Petit Cratère (BPC). **c** Well-rounded primary melt inclusions in olivine from Petit Cratère basalts (PC). A single gas bubble is present. **d** Well-rounded primary melt inclusions in an olivine crystal from the Plaine des Sables fall (PdS). Many gas bubbles are present in the melt inclusion. Note the presence of a trail of micro-fluid inclusions that could indicate a potential volatile leakage from melt inclusions



post-trapping processes as H₂O loss by diffusion across olivine crystals (Massare et al. 2002; Gaetani and Watson 2002; Bucholz et al. 2013) and/or (2) pre-trapping processes affecting magmas (Baker et al. 2005; Spilliaert et al. 2006; Witham 2011). In our case,

(1) We show that no correlation is observed between H₂O content, FeO_T content, and PEC percentage for the melt inclusions discussed in our study (Appendix 6a). That minimizes the role of H₂O loss by reequilibration and/or diffusion across olivine crystals (Danyushevsky et al. 2000; Gaetani and Watson 2002; Massare et al. 2002;

Bucholz et al. 2013; Albert et al. 2019). Water loss can be discarded in our study by considering the absence of daughter minerals in melt inclusions and the primitive nature of the entrapped melt (Sobolev and Chaussidon 1996).

(2) The initial dehydration can thus preferentially be attributed to processes affecting melts before their trapping as melt inclusions like (i) mixing between deep primitive gas-rich melts and shallower more evolved degassed melts (Witham 2011; Myers et al. 2014), (ii) disequilibrium degassing (Baker et al. 2005; Gonnermann and Manga 2005; Pichavant et al 2013;

Table 3 Reconstruction of the initially dissolved CO₂ content in melt inclusion taking into account single shrinkage gas bubbles (see Methods for details about the protocol)

		Peripheral eruptions											
		Primitivite transitional basalts with an alkaline-affinity											
Sites		Trous Blancs (TB)					Below Petit Cratère (BPC)					Piton Chisny (CHI)	
Label		TB047-4-MI1	TB047-5-MI1	TB047-5-MI2	TB047-7-MI1	TB047-7-MI2	TB047-9-MI2	PCR1 ec 51a	BPC-1	BPC-2	BPC-3	BPC-4	PDS2-126
Shrinkage bubble volume	$T_{\text{melt inclusion}} (^{\circ}\text{C})$	1207	1319	1319	1291	1280	1281	1250					1237
	$T_{\text{glass}} (^{\circ}\text{C})$	1204	1204	1204	1204	1204	1204	1217					1213
	Calculated volume shrinkage bubble (%)	0.0	1.9	1.9	1.4	1.2	1.2	0.5					0.4
CO₂ exsolved in shrinkage bubble	Estimated volume shrinkage bubble (%)		1.7		1.6								
	CO ₂ density in shrinkage bubble (g.cm ⁻³)	0.07	0.24	0.33	0.17	0.18	0.36	0.17					0.10
	Glass density (g.cm ⁻³)	2.66	2.72	2.72	2.67	2.66	2.63	2.66	2.66				2.67
Estimated CO₂ dissolved in glass	CO ₂ in shrinkage bubble (ppm)	13	1675	2303	907	840	1729	343					283
	CO ₂ uncertainty (ppm)	86	458	526	349	333	478	229					224
	Pressure of exsolution (bar)	200	850	1250	560	590	1360	550					300
Initial CO₂ in melt inclusion	H ₂ O in glass (wt%)	1.1	1.0	0.4	1.1	1.2	1.2	1.2	1.2	1.1	1.3	0.7	1.1
	CO ₂ in glass (ppm)	0	217	726	99	103	616	57	1456	1518	1416	884	0
	CO ₂ uncertainty (ppm)	130	152	203	140	140	192	136	146	152	142	88	130
Total uncertainty	CO ₂ content (ppm)	13	1892	3029	1006	943	2345	400	1456	1518	1416	884	283
	Total uncertainty (ppm)	156	482	564	376	361	515	266	146	152	142	88	259

Font in italic, measurements performed by FTIR. In bold, reconstructed CO₂ content

Fig. 7 Composition in major elements of melt inclusions, corrected for PEC, and matrix glasses. **a** MgO vs. CaO/Al₂O₃ with the distinct groups of lavas usually defined at Piton de la Fournaise (Lénat et al. 2012; Valer et al. 2017). **b** Alkalinity index AI vs. CaO/Al₂O₃. **c** SiO₂ vs. K₂O. Grey area is the composition range of melt inclusions and matrix glasses from the 1998–2010 central products. The compositions of ultramafic enclaves are pointed by the black arrows (D, dunite; W, wehrlite; G, gabbros). Dashed lines are predicted melt evolution following a wehrlitic differentiation trends. Numbers represent the forsterite contents of the hosting olivine crystals

Yoshimura 2015), and/or (iii) CO₂ flushing affecting dissolved volatile ratios (Spilliaert et al. 2006; Collins et al 2009; Blundy and Cashman 2008; Métrich et al. 2010). On the one hand, the absence in our dataset on melts emitted along the NWRZ of reverse correlation between H₂O and K₂O contents (Fig. 9b) permits to exclude the role of magma mixing between primitive gas-rich melts and more evolved-degassed melts. On the other hand, the slight correlation ($R^2 = 0.55$) between H₂O and S contents (Appendix 6b) does not support the hypothesis of a disequilibrium degassing due to the low diffusivity of S with respect to H₂O and CO₂ in basaltic melts (Pichavant et al. 2013). Conversely, Boudoire et al. (2018) have recently highlighted that about 68 wt% of the initial CO₂ in Piton de la Fournaise melts is already exsolved in the upper mantle, as expected owing the CO₂ dependence on the pressure (Métrich et al. 2014; Di Muro et al. 2016). We stress that massive early-stage CO₂ exsolution may percolate within the upper part of the plumbing system and increase the CO₂/H₂O ratio with respect to the equilibrium degassing trends.

Our combined barometric results from fluid inclusions and melt inclusions make the mantle-crust underplating layer the locus of magma ponding and degassing beneath the NWRZ (Bureau et al. 1998a; Liuzzo et al. 2015; Boudoire et al. 2018), favouring CO₂/H₂O increase in magmas as recorded by melt inclusions in olivine crystals from peripheral lavas emitted along the NWRZ.

Alkali enrichment by degassing-induced clinopyroxene crystallization and mixing between variably evolved melts

The role of clinopyroxene in controlling the deep and early evolution of Piton de la Fournaise magmas has been extensively discussed since the pioneering work of Albarède et al. (1997). We have shown that the trend of alkali enrichment recorded by evolved melt inclusions and mostly in matrix glasses occurs together with CaO/Al₂O₃ decrease and SiO₂ enrichment. A similar trend of evolution was documented for bulk rocks at Piton de la Fournaise and attributed to the role

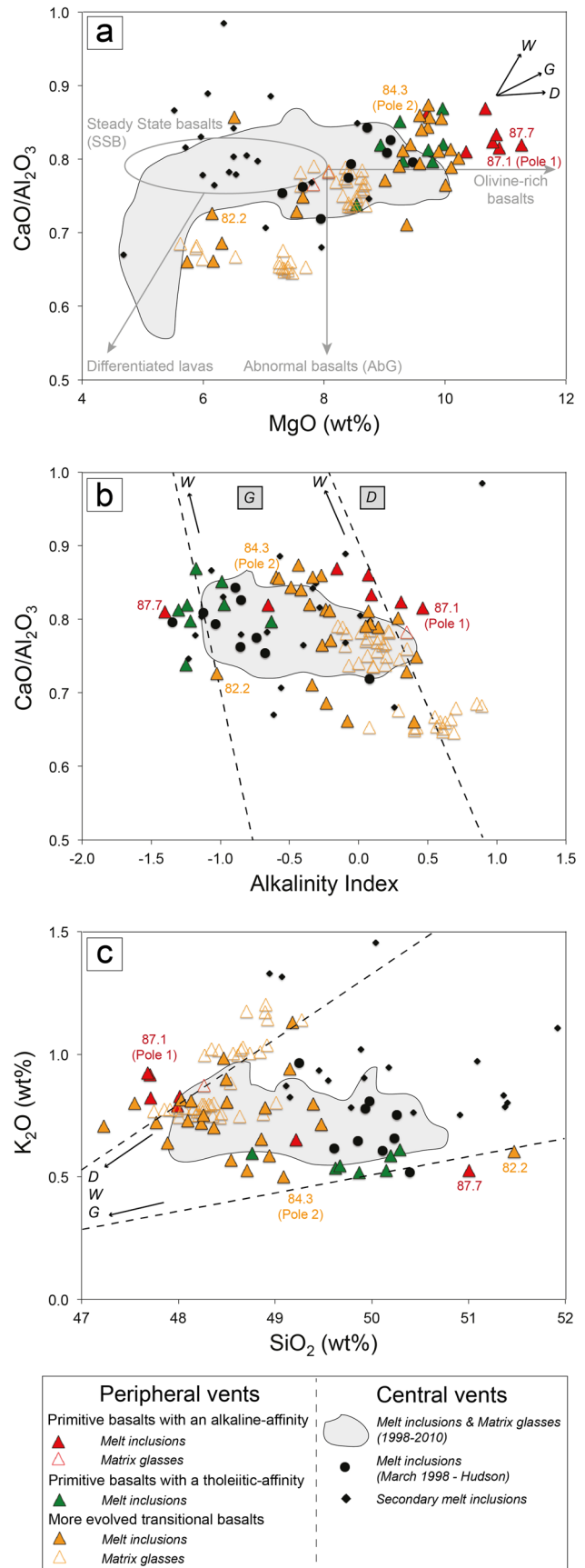


Table 4 Recalculated melt inclusions composition, CO₂-H₂O saturation pressure (Duan 2014), and elemental ratios. 87.1, 86.2, 87.7, 84.3, and 82.2 individual composition mark geochemical poles described in this study (see text for explanation)

Major element (wt%)	Peripheral eruptions														
	Primitive transitional basalts					More evolved transitional basalts									
	Alkaline affinity (TB)					Tholeiitic affinity (PdC)									
	Average (n = 5)	σ	87.1 (Pole1)	86.2	87.7	Average (n = 12)	σ	(BPC - PC - HA - PdS)	84.3 (HA) (Pole 2)	82.2 (PC)	Average (n = 9)	σ	1998-2010 (98-10)	Average (n = 116)	σ
SiO ₂	48.1	0.6	47.7	48.0	49.2	50.1	0.9	48.6	49.1	51.5	50.0	0.4	49.5	1.1	
K ₂ O	0.8	0.1	0.9	0.8	0.7	0.6	0.2	0.7	0.5	0.6	0.7	0.1	0.8	0.2	
Na ₂ O	2.5	0.2	2.8	2.6	2.5	2.4	0.1	2.4	2.6	3.0	2.5	0.2	2.6	0.2	
TiO ₂	2.6	0.1	2.6	2.5	2.4	2.7	0.2	2.7	2.4	2.5	2.7	0.2	2.7	0.2	
MgO	10.7	0.6	10.9	10.9	11.3	9.4	0.5	8.8	9.7	6.1	8.5	0.7	7.9	1.0	
FeO _T	11.1	0.8	10.6	11.4	10.2	10.2	0.8	11.4	11.6	9.1	9.6	0.7	10.6	1.1	
CaO	10.9	0.3	10.8	10.7	10.5	10.8	0.2	10.9	10.9	11.3	11.2	0.5	11.0	0.7	
Al ₂ O ₃	12.9	0.3	13.3	12.8	12.8	13.3	0.6	13.9	12.7	15.5	14.3	0.4	14.3	0.7	
P ₂ O ₅	0.3	0.0	0.3	0.3	0.3	0.2	0.1	0.3	0.3	0.2	0.3	0.1	0.8	0.2	
Volatiles															
Cl (ppm)	299	46	338	259	244	249	42	306	184	247	331	43	269	50	
S (ppm)	1842	1142	1706	1636	1525	1333	318	1556	1889	1297	1347	506	1032	237	
H ₂ O (wt%)	0.9	0.4	1.4	1.2	1.2	1.0	0.2	1.1	1.0	1.0	1.2	0.5	0.8	0.2	
CO ₂ (ppm)	1671	1081	nd	1188	nd	1188	337	1024	nd	nd	2207	1119	95	39	
Ratios															
CaO/Al ₂ O ₃	0.84	0.02	0.82	0.83	0.82	0.81	0.04	0.79	0.86	0.73	0.79	0.04	0.77	0.04	
Alkalinity index	0.15	0.39	0.47	0.09	-0.65	-1.10	0.22	-0.18	0.35	-0.59	-0.83	0.40	-0.56	0.36	
K ₂ O/TiO ₂	0.33	0.03	0.35	0.31	0.27	0.24	0.11	0.28	0.21	0.25	0.26	0.04	0.28	0.06	
K ₂ O/ P ₂ O ₅	2.73	0.11	2.69	2.64	2.34	2.17	0.21	2.40	1.74	2.90	2.46	0.87	2.01	0.33	
Cl/K ₂ O	0.039	0.005	0.037	0.033	0.021	0.038	0.004	0.042	0.005	0.037	0.048	0.002	0.037	0.007	
Pressure															
Melt inclusions	2.7	1.4	nd	2.1	nd	3.0	0.5	2.1	nd	nd	4.0	1.6	0.4	0.1	
Fluid inclusions	3.5	0.4	nd	nd	nd	4.5	nd	2.7	1.1	nd	<4.4	nd	<1.5	nd	

Font in bold, CO₂-H₂O saturation pressure calculations in melt inclusions that take into account the CO₂ content trapped only in single gas bubbles hosted in melt inclusions (see Table 3), nd, not determined

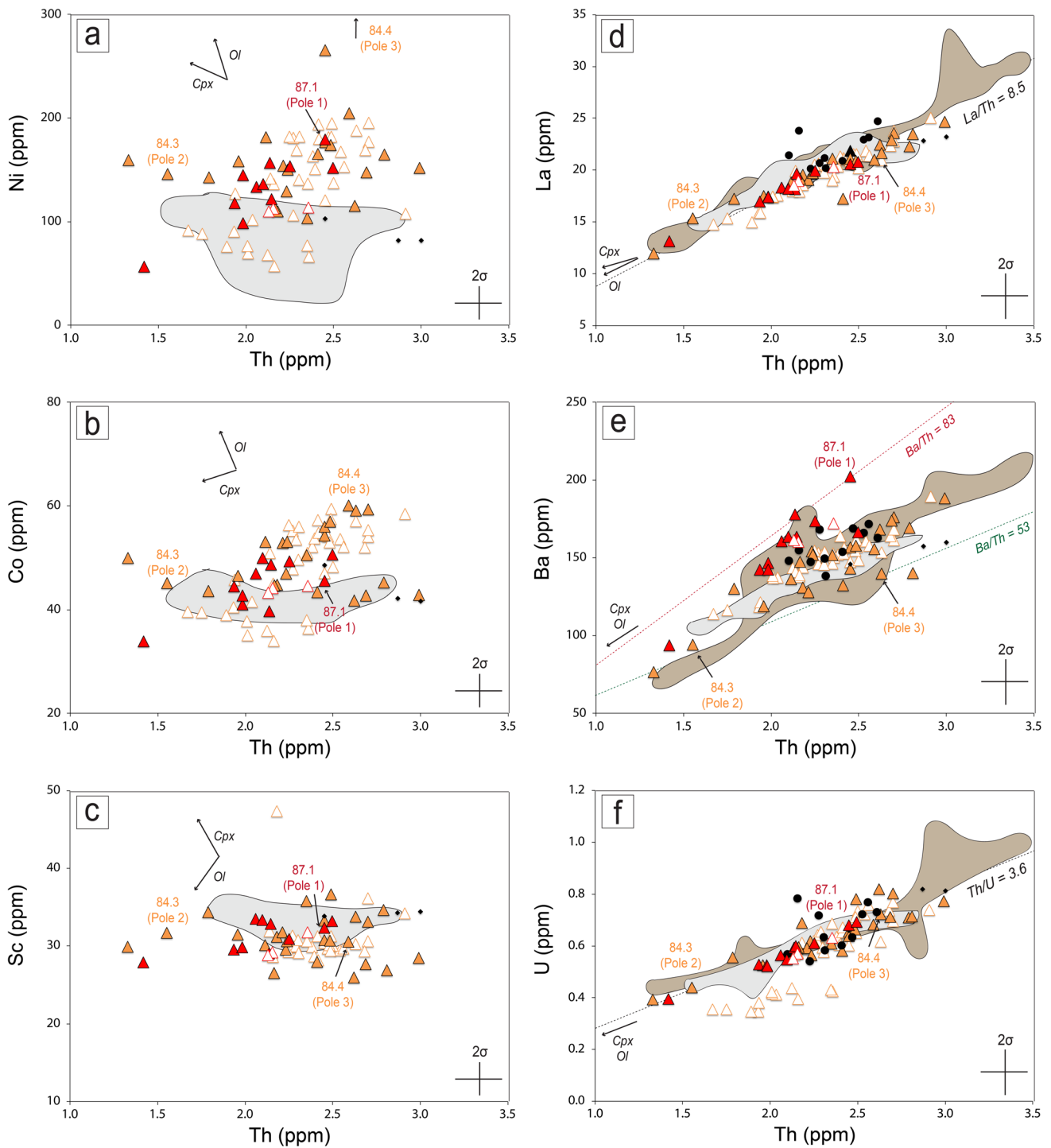


Fig. 8 Composition in compatible (a, b, c) and incompatible (d, e, f) trace elements from melt inclusions and matrix glasses. Clinopyroxene and olivine composition from Appendix 1. Intersection of dotted lines at 0. Same symbols and legend as in Fig. 7. Grey areas are melt

of late clinopyroxene fractionation (Boudoire et al. 2019). Our study of melt inclusions and in particular of dissolved volatile elements provides a new look on the conditions of deep clinopyroxene stability in the range 3–6 kbar and its

inclusion compositions in olivine crystals from central products from the major April 2007 caldera forming eruption (Di Muro et al. 2014). Data from peripheral basalts (brown filled area) from Valer (2016) and Valer et al. (2017)

link with the observed enrichment in alkalis in Piton de la Fournaise residual melts.

With respect to the initial melt composition calculated by Boudoire et al. (2019) and used to model melt evolution

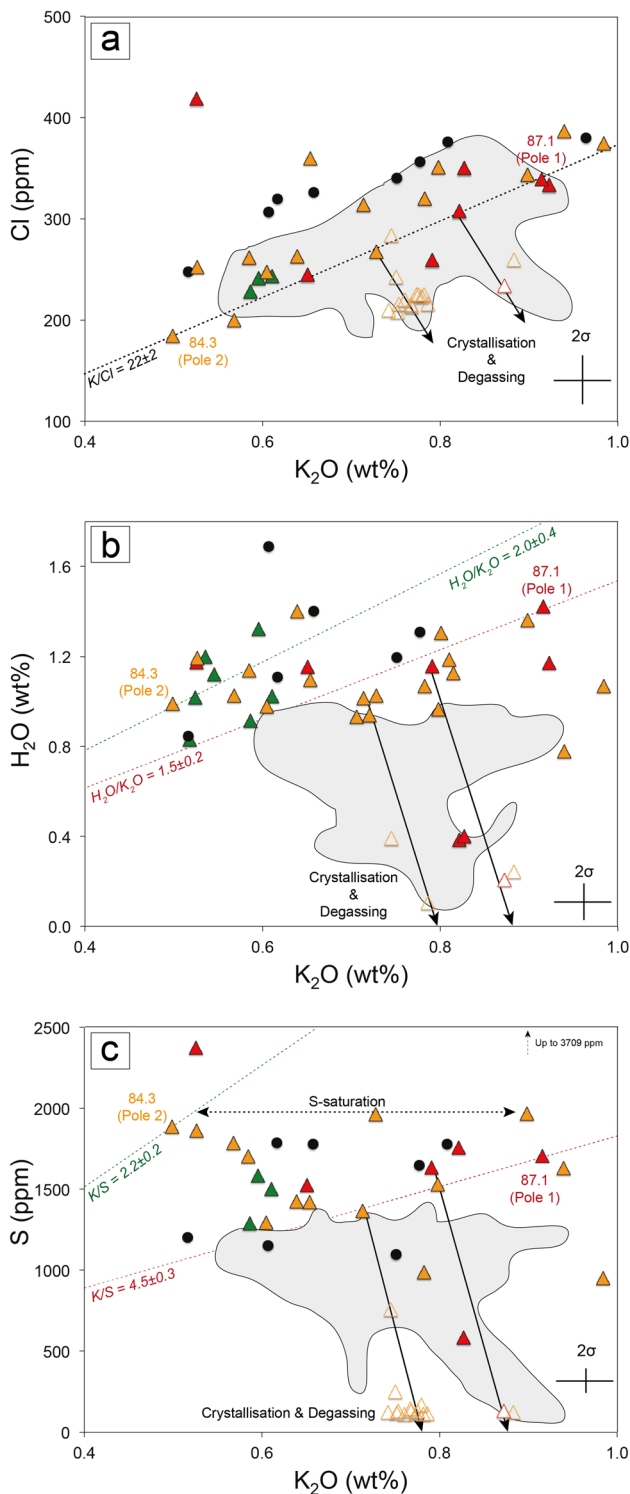


Fig. 9 Dissolved volatile contents in melt inclusions (recalculated) and matrix glasses. **a** K_2O vs. Cl. **b** K_2O vs. H_2O . **c** K_2O vs. S. Grey area is the composition range of melt inclusions and matrix glasses from the 1998–2010 central products. Same symbols as in Fig. 7. The “crystallization and degassing” trends fit melt inclusions and related matrix glasses with respect to the differentiation trends defined in Fig. 7

at Piton de la Fournaise (AlphaMELTS code; Asimow et al. 2003; Ghiorso et al. 2001; Ghiorso and Sack 1995), we model here the evolution of PdF magmas starting from most magnesian melt inclusion documented in our study (inclusion $Fo_{87.7}$ in TB; $H_2O = 1.4$ wt%; Table 4). Oxygen fugacity was fixed at NNO-0.5 based on the review of Piton de la Fournaise melts made by Pichavant et al. (2016). Nevertheless, oxygen fugacity variability is not expected to play a major role in the Piton de la Fournaise fractionation sequence (Boudoire et al. 2019). Initial temperature (1280 °C) was estimated from the MgO thermometer of Helz and Thornber (1987) modified by Putirka (2008). The results of a simulated simple fractionation process (red lines on Fig. 11a) highlight that olivine is the first phase to crystallize and clinopyroxene appears at 1190 °C (6 kbar) and 1140 °C (3 kbar) in H_2O -rich melts (1.6 wt%). While these trends fit the composition of lavas from NWRZ peripheral vents (Boudoire et al. 2019), they do not fit the composition of more evolved melt inclusions and matrix glasses described in this study. Conversely, in more dehydrated melts, i.e. $H_2O = 0.4$ – 0.5 wt%, like the most water-poor melt inclusions (Fig. 10b), clinopyroxene starts fractionating at higher temperature, between 1230°C (at 6 kbar) and 1180°C (at 3 kbar). Modelled differentiation trends (blue lines on Fig. 11a) better fit with most of water-poor evolved melt inclusions and matrix glasses and overlap uncorrected composition of melt inclusions in TB clinopyroxenes (Fig. 11a; Appendix 3). Our modelling supports the idea that decrease in dissolved water at high pressure, possibly induced by extensive CO_2 flushing at the depth of the mantle-crust underplating layer can play a major role to control the stability of clinopyroxene with respect to olivine. Conversely, inputs of hot volatile-rich melts can destabilize and dissolve the early formed clinopyroxene (Boudoire et al. 2019). This process is fully consistent with recent experimental studies made on Piton de la Fournaise melts (Brugier 2016) and resorption textures observed in clinopyroxene crystals (Fig. 5). We thus corroborate our early findings (Boudoire et al. 2019) showing that the alkali enrichment associated with low CaO/Al_2O_3 observed in some low magnesian ($MgO < 9$ wt%) matrix glasses and melt inclusions (Figs. 7b, 10a) is triggered by clinopyroxene fractionation in dehydrated melts ponding at the depth of the mantle-crust underplating layer and at shallower levels.

We also document a few melt inclusions with variable CaO/Al_2O_3 at intermediate MgO contents (9–10 wt%) that do not fall on the crystallization trends modelled in the 3–6 kbar pressure range (Fig. 11a). These compositions may track (1) a deeper step of clinopyroxene dissolution/crystallization (>6 kbar) and/or (2) the effect of magma mixing between deep primitive and more evolved melts (Fig. 11a):

◀**Fig. 10 a** Pressure distribution from fluid inclusions barometry from NWRZ (in black) and central (in grey) lavas (46 measurements in this study and 53 analysis from Boudoire et al. (2019)). Piton de la Fournaise interfaces depth as in Boudoire et al. (2019). Underp., underplating layer at the mantle-crust transition. **b** Comparison between melt inclusion compositions (H_2O and CO_2) analysed and recalculated with different methods (FTIR-SIMS, Raman; see text for explanation and Table 3). Grey area is the composition range of melt inclusions and matrix glasses from the 1998–2010 central products: only melt inclusions in olivine crystals from the central Hudson (H) basalts are enriched in CO_2 (highlighted with grey circles). Melt inclusions in olivine crystals from NWRZ lavas are shown with triangles. Main pressure modes from fluid inclusion barometry in crystals from NWRZ and central basalts are reported (see a). Isobars calculated from Duan (2014). Open-system (OS)/closed-system (CS; exsolved vapour phase = 1 wt%) degassing paths calculated from Duan (2014). Error bars for each melt inclusion represent the cumulated uncertainty resulting from the methodology of CO_2 recalculation developed in this study (see Methods)

- (1) High CaO/Al_2O_3 ratios (mostly linked to an impoverishment in Al_2O_3) are found in melt inclusions hosted in Fo_{83-86} olivine crystals rather than in $Fo_{>86}$ olivine crystals. This does not support the hypothesis of an early effect of deep (>6 kbar) clinopyroxene crystallization but instead of the process of clinopyroxene dissolution during magma recharges discussed in Boudoire et al. (2019) (Fig. 11a; Appendix 6c).
- (2) Our petrological investigation on olivine and clinopyroxene crystal zoning better supports the hypothesis of magma mixing between deep primitive and more evolved melts (Fig. 11a). Actually, the most evolved melts measured (cf PC) and modelled in our study are in equilibrium with Fo_{80-82} olivine crystal (Fig. 11a) recording reverse zoning (Fig. 3). Moreover, their clinopyroxenes display melt inclusions with a negative PEC, and both resorption surface (Fig. 5) and Mg-Cr-rich bands (Fig. 5) are hardly attributable to (i) crystal growth effect (Mg and Cr being anticorrelated in sector zoned clinopyroxenes; Kouchi et al. 1983; Mollo et al. 2010; Hammer et al. 2016) and/or (ii) convective thermal effect expected to generate an alternance between Mg-Cr-rich bands (hotter conditions) and Ti-rich zones (cooler conditions; Danyushevsky et al. 2000; Welsch et al. 2009; Johnson et al. 2010; Head et al. 2011). We attribute the oscillatory zoned clinopyroxene rims (Fig. 5) to a convective effect during magma transfer (in dykes or sills) as suggested by the progressive Ti/Al ratio increase in rims (barometric proxy; Boudoire et al. 2019).

Thus, magma ponding at the depth of the mantle-crust underplating layer (ca. 4 kbar) plays a major role in the geochemical melt variability at Piton de la Fournaise

by combining the competitive effects of crystallization-dehydration processes, magma mixing between variably evolved melts, and recycling or even assimilation of pre-existing crystals (Fig. 11b). There, melt dehydration and clinopyroxene crystallization/dissolution control the alkali enrichment and CaO/Al_2O_3 variability reported in lavas emitted in the NWRZ (Lénat et al. 2012; Valer et al. 2017; Boudoire et al. 2019). Conversely, intermediate melt compositions, as recorded by steady state basalts emitted in the central area, record effective mixing of magmas injected in the central and shallower crustal reservoir. Mixing is responsible of hiding potential pristine alkali enrichment (Fig. 11b) and leads to the emission of evolved and hybrid lavas as commonly observed at oceanic basaltic volcanoes (Di Muro et al. 2014; Schipper et al. 2015, 2016; Jennings et al. 2017).

Alkali enrichment by partial melting of a slightly heterogeneous mantle source and contamination with low-degree partial melts derived from cumulates

Besides the main trend in alkali enrichment, together with CaO/Al_2O_3 decrease and SiO_2 enrichment, measured in some evolved melts and matrix glasses and tracking the effect of late-stage clinopyroxene fractionation, we have also documented at Piton de la Fournaise alkali enrichment in high magnesian melt inclusions, i.e. for primitive melts. Interestingly, these high magnesian ($MgO > 10$ wt%) melt inclusions have a highly variable alkali and SiO_2 contents at constant CaO/Al_2O_3 ratio (inclusions $Fo_{87.7}$ and $Fo_{87.1}$; Fig. 7). They support the role of magmatic processes in the chemical variability of the melts of Piton de la Fournaise other than the crystallization of deep clinopyroxene invoked by Albarède et al. (1997).

On one side, the enrichment in major (K_2O , Na_2O) and trace (Ba, Rb) alkali elements in some inclusions (Pole 1) correlates with an enrichment in incompatible trace elements (La, Th) and Cl and a depletion in SiO_2 (Fig. 7, 8, 9) that could be attributed to a lower melting degree of the source (Reiners and Nelson 1998; Bourdon et al. 2005). We used a batch melting model based on the composition of a primitive mantle (Wang et al. 2018) at 3 GPa composed by 53% olivine, 34% clinopyroxene, 8% orthopyroxene, and 5% garnet as previously discussed by Valer et al. (2017) for La Réunion magmas. Crystal-melt partition coefficients are from Salters and Stracke (2004). Through this model, we estimate that part of the observed geochemical variability (as recorded by melt inclusions in magnesian inclusions like Pole 1 on Fig. 12a, b) could be explained by a variation of the degree of partial melting from 5 to 7%. Higher melting degrees, 8–10%, are recorded in melt inclusions with a tholeiitic

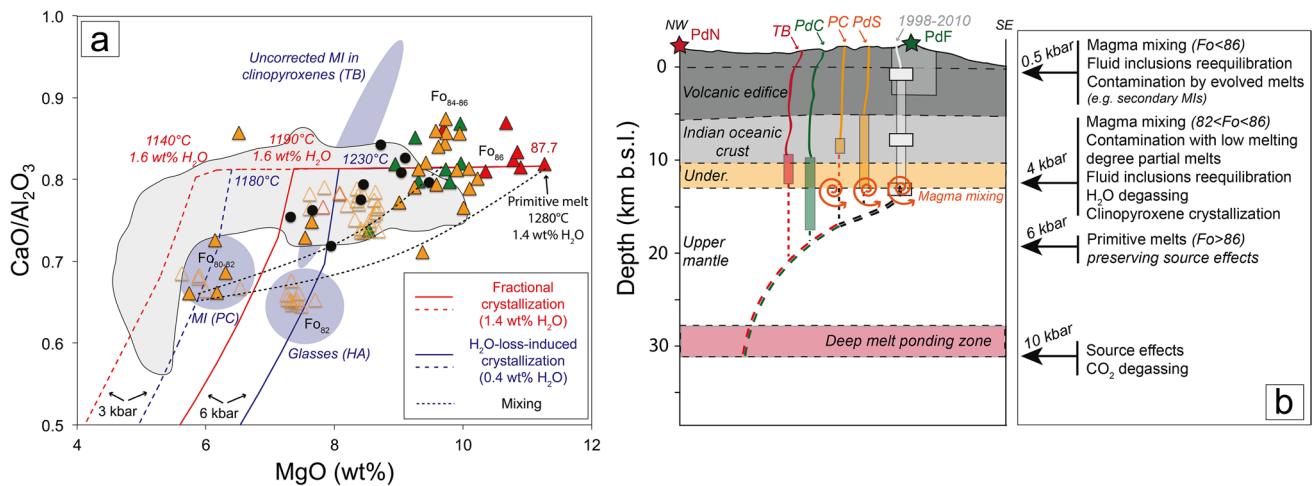


Fig. 11 a AlphaMELTS simulations of crystallization paths taking into account the potential effect of water loss induced by CO₂ flushing. Starting melt corresponds to the most primitive composition found in the melt inclusions described in this study (inclusion Fo_{87.7}; TB). Oxygen fugacity is fixed at NNO-0.5 in accordance with recent review of Piton de la Fournaise melts (Pichavant et al. 2016). Starting

signature (Pole 2) and in central magmas like those of the large April 2007 eruption. This range of degrees of partial melting is fully consistent with those previously reported at La Réunion (Ludden 1978; Albarède and Tamagnan 1988; Valer et al. 2017; Vlastélic et al. 2018).

On the other side, variable degrees of partial melting of a homogenous mantle source fail to explain the variations of some canonical ratios of highly incompatible elements like Nb/U, Ba/Th, and Ce/Pb in melts with either a tholeiitic or an alkaline affinity (Fig. 12c, d; Appendix 7). This is even more true considering that such variations may occur at variable Ba/Th contents and La/Yb ratios (between Pole 1 and Pole 2 on Figs. 8 and 12, respectively). Together with the enrichment in radiogenic Sr of some lavas with an alkaline affinity (Table 1), these observations better support the role of some minor source heterogeneities (Huang et al. 2005; Workman and Hart 2005; Jackson and Dasgupta 2008; Vlastélic et al. 2018). At La Réunion, source heterogeneity was invoked to explain (i) the correlation between Sr isotopes and ratios of variably incompatible trace elements as Th/Yb (Fig. 12b; Di Muro et al. 2014; Vlastélic et al. 2018; Boudoire et al. 2019) and (ii) the Nd-Hf-Pb variability observed between the old dormant Piton des Neiges volcano and the currently active Piton de la Fournaise volcano (Bosch et al. 2008; Nauret et al. 2019). Melt extraction from small-scale distinct mantle components within the plume characterized by variable canonical ratios (Ba/Th, Th/Yb on Figs. 8 and 12) and Sr isotope signature may explain the geochemical variability in trace elements described in high magnesian melt inclusions (black arrows on Fig. 12). Interestingly, a

temperature was computed from the hydrous melt composition by the equation of Putirka (2008). Same symbols as in Fig. 7. **b** Conceptual model of the deep plumbing system of Piton de la Fournaise showing magma evolution below the NW rift zone (modified from Boudoire et al. (2019); see Boudoire et al. (2019) for explanation about the relation between pressure and depth beneath La Réunion island)

compilation of bulk rock data from basalts and mugearites of Piton de la Fournaise and Piton des Neiges late-stage activity (Younger Lavas; Smietana 2011) shows that, on average, (i) high magnesian melt inclusions with a tholeiitic affinity and marked by low Nb/U, Nb/Y, and Ba/Th ratios (Pole 1) mirror the composition of the lava emitted during the large 2007 caldera-forming event of the 5th April 2007 at Piton de la Fournaise whereas (ii) those with an alkaline affinity and marked by high La/Yb, Nb/U, Nb/Y, and Ba/Th ratios (inclusion Fo_{87.1}) are geochemically close to the composition of late-stage lavas emitted by the Piton des Neiges volcano (Fig. 12c; Appendix 7). As peripheral products investigated in our study lie on the NWRZ, i.e. the rift zone linking Piton des Neiges and Piton de la Fournaise volcanoes, these geochemical signatures raise major issues regarding the current magmatic activity of both PdF and PdN plumbing systems (Fig. 11b).

Noteworthy, we have documented some evolved melt inclusions (Pole 3) that are even more enriched in some highly incompatible elements (Th, U, La) than the geochemical poles described above (Fig. 8). In these melt inclusions, the selective increase in Th and U leads to lower Ba/Th and Nb/U ratios, respectively (Fig. 12c, d). Such observation contrasts with previous findings attributing the variability of these ratios only to source processes at Piton de la Fournaise (Valer et al. 2017). Instead, this behaviour reflects a possible effect of mixing between mantle-derived magmas and low-degree partial melts derived from cumulates having experienced an enrichment in fluid mobile elements (Bureau et al. 1998a; Pietruszka

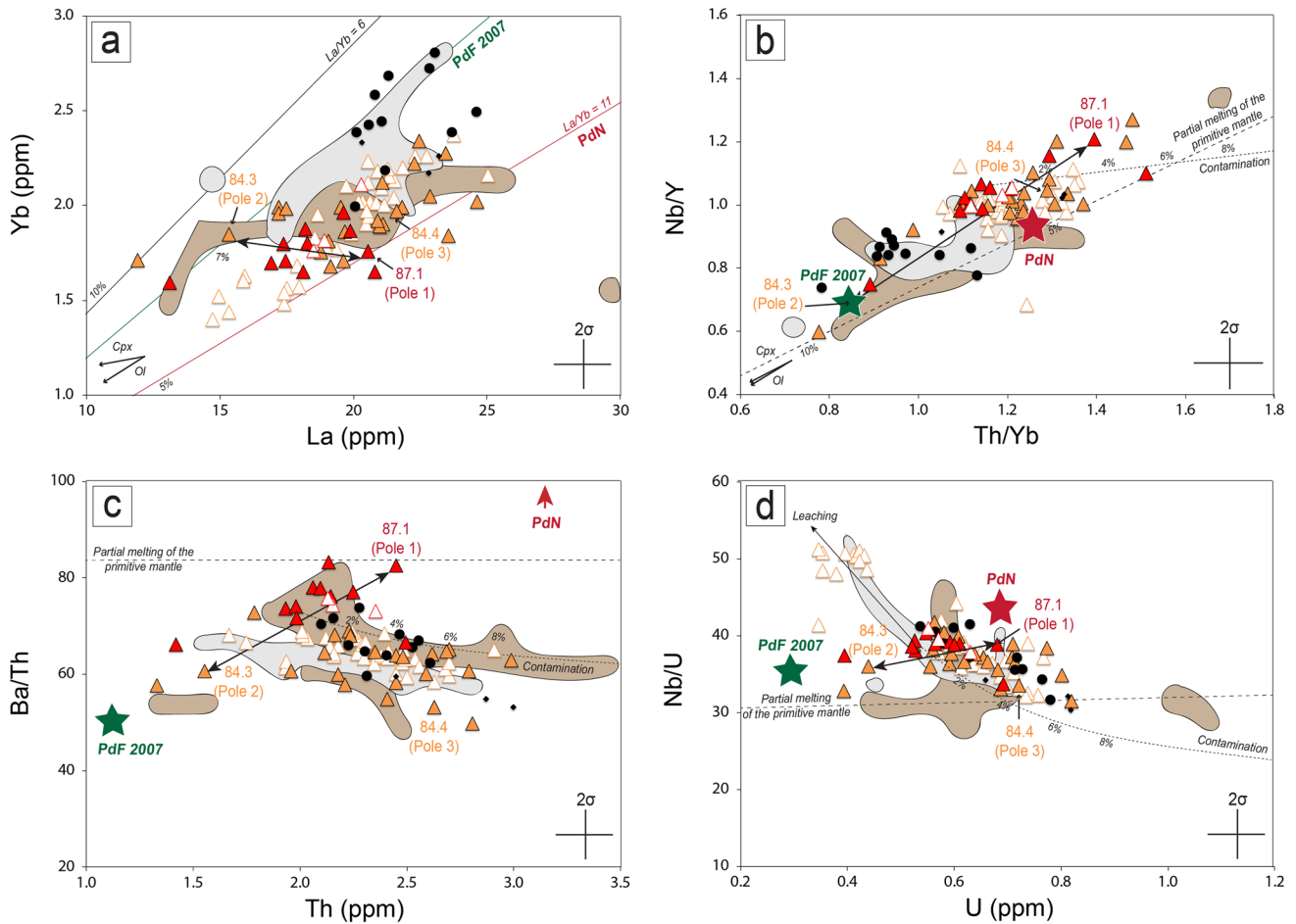


Fig. 12 Concentration and ratios in variably incompatible trace elements in melt inclusions and matrix glasses. Same symbols and legend as in Figs. 7 and 8. The clinopyroxene and olivine compositions are indicated by the black arrows (Appendix 1). Continuous green line (intersection at 0) and star fit the bulk rock composition of the low radiogenic Sr basalt of the 5th April 2007 (Di Muro et al. 2014). Continuous red line (intersection at 0) and star fit the average composition of the late-stage lavas of the currently dormant Piton des Neiges volcano (younger lavas <350 kyrs; Smietana 2011). Black dashed line represents the expected variability of melt compositions

related to various degrees of partial melting (italic numbers) applying a modal batch melting of a garnet peridotite solid source (see Valer et al. (2017) for explanations: starting conditions from Wang et al. (2018)). Black arrows highlight the effect of source heterogeneities on the variability in trace elements. The black dotted line represents the expected variability of melt compositions related to assimilation of 1% of a partial melt from wehrlite cumulate (see text for explanations; initial conditions: “94.G1” cumulate from Upton et al. (2000); coefficients of partition between melt-olivine-clinopyroxene at 1 GPa and 1200 °C from Adam and Green (2006))

et al. 2009; Boudoire et al. 2019). To test this hypothesis, we have calculated the mixing of:

- (1) A melt with a composition intermediate between those found in Pole 1 and Pole 2 (“TB047-8-2” in Appendix 3) as expected by the formation of hybrid magmas at the depth of the mantle-crust underplating layer (Fig. 10a)
- (2) A melt produced by low degree ($\approx 1\%$; Pietruszka et al. 2009; Boudoire et al. 2019) of partial melting from a standard (i.e. not enriched) wehrlite cumulate (“94.G1”; Upton et al. 2000; Boudoire et al. 2019). Wehrlite cumulates, together with dunite cumulates, are expected to represent the composition of the dense

layer of underplated material (Pietruszka et al. 2009) related to the crystallization of magmas ponding at the mantle-crust interface (Charvis et al. 1999; Fontaine et al. 2015).

The simulated mixing curves show that the contamination of mantle-derived melts with such partial melts from wehrlite cumulates may lead to an enrichment in incompatible trace elements (Th, U) together with a decrease of the Ba/Th and Nb/U ratios as observed in part of the evolved melt inclusions (Pole 3) and secondary melt inclusions (Fig. 12b, c, d; Bureau et al. 1998a; Di Muro et al. 2014). We calculate that less than 2% of assimilation of partial melt from wehrlite cumulates is required to explain most of the enrichment

in trace elements of these evolved melt inclusions. Meanwhile, a larger degree of assimilation (up to 10%) of partial melt is required to explain the most enriched compositions. As suggested by Pietruszka et al. (2009), enrichment in Th and U of the assimilated melts can explain these extreme compositions.

Previous studies at Piton de la Fournaise have highlighted the role of U remobilization in bulk rock (Albarède et al. 1997; Pietruszka et al. 2009; Vlastélic et al. 2011) and melt inclusions (Di Muro et al. 2014) related to a leaching and transfer by either meteoritic-hydrothermal water or by magmatic fluids. On the one hand, we measure the highest Nb/U ratios in part of the matrix glasses (Fig. 12d), and this process could be related to late-stage U leaching by meteoritic waters during weathering (Aiuppa et al. 2000) or by acidic gas in fumarolic environment (Vlastélic et al. 2011). However, the unaltered appearance of those glasses and the absence of systematic SiO₂ enrichment together with a decrease in Al₂O₃, MgO, and FeO_T minimize the role of late-stage hydrothermal alteration (Vlastélic et al. 2011). On the other hand, the U enrichment recorded in some evolved melt inclusions occurs (i) independently of the composition in major elements and (ii) together with an enrichment in Th and La leading to constant U/Th and La/Th ratios (Fig. 8). These results exclude a contamination by late-stage acidic gases or by meteoritic waters to explain the observed chemical variability (Aiuppa et al. 2000; Vlastélic et al. 2011). Instead, we suggest that cumulates located at the depth of the mantle-crust underplating layer (i.e. preserved from interaction with meteoritic waters) may be metasomatized by deep (mantle) magmatic fluids enriched in a range of elements as U, Th, La (Hedenquist and Lowenstern 1994; Pietruszka et al. 2009), and radiogenic He produced by U-Th radioactive decay (Boudoire et al. 2020). We speculate that this process may be favoured by the occurrence of CO₂-rich fluids in the upper mantle beneath Piton de la Fournaise and in particular at the depth of mantle-crust underplating layer (Lowenstern (2001) and references therein).

Conclusion

In this study, we characterize for the first time crystal zoning, fluid and melt inclusions composition, and barometry in olivine and clinopyroxene crystals from fast quenched mafic basalts having an alkaline affinity and emitted along the North-West rift zone linking Piton de la Fournaise and Piton des Neiges volcanoes. We document here the most primitive melt inclusions found so far on La Réunion (MgO = 11.3 wt%), and we show that alkaline enrichment in melts emitted from peripheral vents is mainly related to the competitive effects between (1) various degrees of partial melting

of a slightly heterogenous mantle source and (2) late-stage clinopyroxene crystallization at the depth of the mantle-crust underplating layer. We suggest that deep pyroxene stability is controlled by magma water content and melt dehydration by extensive CO₂ flushing.

We show that the mantle-crust underplating layer is a major site of magma evolution and that magma ponding at that depth (10–15 km below sea level) experiences (i) CO₂ flushing and increase in CO₂/H₂O ratios, (ii) mixing between melts recording slight source heterogeneity, (iii) crystal recycling/assimilation, and (iv) contamination with low-degree partial melts from metasomatized cumulates. Magma mixing is even more advanced for melts ascending in the crustal part of the volcano plumbing system, leading to the apparent geochemical homogeneity of evolved and degassed melts emitted in the central area during the frequent activity of Piton de la Fournaise.

Primitive melts in magnesian-rich unzoned olivine (Fo_{>86}) provide snapshots of the mantellic part of the plumbing system (>15 km below sea level) and record a range of geochemical signatures that lie between that of the current activity of Piton de la Fournaise and that of the late-stage activity of the quiescent neighbouring Piton des Neiges volcano. These findings raise major issue regarding the activity of the NWRZ linking both volcanoes and more generally on the current magmatic activity below the whole island.

Supplementary Information The online version contains supplementary material available at <https://doi.org/10.1007/s00445-021-01508-6>.

Acknowledgements We acknowledge helpful technical support from N. Braukmüller, A. Kronz, G. Labeau, G. Montagnac, and D. Neuville during microanalysis. V. Zanon is gratefully acknowledged for stimulating discussions on ocean island magmatism. We are in debt with C. Sundermeyer and G. Wörner for the analytical support and constructive discussions.

Funding The Université de La Réunion and the ANR “STRAP” (ANR-14-CE03-0004) have funded this work. We also acknowledge the French government IDEX-ISITE initiative 16-IDEX-0001 (CAP 20-25). This is Laboratory of Excellence ClerVolc contribution number 508.

References

- Adam J, Green T (2006) Trace element partitioning between mica and amphibole-bearing garnet lherzolite and hydrous basanitic melt: 1. experimental results and the investigation of controls on partitioning behaviour. *Contrib Mineral Petrol* 152:1–17. <https://doi.org/10.1007/s00410-006-0085-4>
- Aiuppa A, Allard P, D’Alessandro W, Michel A, Parello F, Treuil M, Valenza M (2000) Mobility and fluxes of major, minor and trace metals during basalt weathering and groundwater transport at Mt. Etna volcano (Sicily). *Geochim Cosmochim Acta* 64:1827–1841. [https://doi.org/10.1016/S0016-7037\(00\)00345-8](https://doi.org/10.1016/S0016-7037(00)00345-8)

- Albarède F, Luais B, Fitton G, Semet M, Kaminski E, Upton BGI, Bachèlery P, Cheminée JL (1997) The geochemical regimes of Piton de la Fournaise volcano (Réunion) during the last 530000 years. *J Petrol* 38:171–201. <https://doi.org/10.1093/etroj/38.2.171>
- Albarède F, Tamagnan V (1988) Modeling the recent geochemical evolution of the Piton de la Fournaise volcano, Reunion Island. *J Petrol* 29:997–1030. <https://doi.org/10.1093/etroj/29.5.997>
- Albert H, Costa F, Di Muro A, Herrin J, Métrich N, Deloule E (2019) Magma interactions, crystal mush formation, timescales, and unrest during caldera collapse and lateral eruption at ocean island basaltic volcanoes (Piton de la Fournaise, La Réunion). *Earth Planet Sci Lett* 515:187–199. <https://doi.org/10.1016/j.epsl.2019.02.035>
- Asimow PD, Dixon JE, Langmuir CH (2003) A hydrous melting and fractionation model for mid-ocean ridge basalts: application to the Mid-Atlantic Ridge near the Azores. *Geochem Geophys Geosyst* 5:Q01E16. <https://doi.org/10.1029/2003GC000568>
- Aster EM, Wallace PJ, Moore LR, Watkins J, Gazel E, Bodnar RJ (2016) Reconstructing CO₂ concentrations in basaltic melt inclusions using Raman analysis of vapor bubbles. *J Volcanol Geotherm Res* 323:148–162. <https://doi.org/10.1016/j.jvolgeores.2016.04.028>
- Baker DR, Freda C, Brooker RA, Scarlato P (2005) Volatile diffusion in silicate melts and its effects on melt inclusions. *Ann Geophys* 48(4-5). <https://doi.org/10.4401/ag-3227>
- Bakker RJ (2003) Package FLUIDS 1. Computer programs for analysis of fluid inclusion data and for modelling bulk fluid properties. *Chem Geol* 194(1-3):3–23. [https://doi.org/10.1016/S0009-2541\(02\)00268-1](https://doi.org/10.1016/S0009-2541(02)00268-1)
- Blundy J, Cashman K (2008) Petrologic reconstruction of magmatic system variables and processes. *Rev Mineral Geochem* 69:179–239. <https://doi.org/10.2138/rmg.2008.69.6>
- Boivin P, Bachèlery P (2009) Petrology of 1977 to 1998 eruptions of Piton de la Fournaise, La Réunion Island. *J Volcanol Geotherm Res* 184:109–125. <https://doi.org/10.1016/j.jvolgeores.2009.01.012> (Elsevier B.V)
- Bosch D, Blichert-Toft J, Moynier F, Nelson BK, Telouk P, Gillot PY, Albarède F (2008) Pb, Hf and Nd isotope compositions of the two Réunion volcanoes (Indian Ocean): a tale of two small-scale mantle blobs. *Earth Planet Sci Lett* 265:748–768
- Bouidoire G (2017) Architecture et dynamique des systèmes magmatiques associés aux volcans basaltiques: exemple du Piton de la Fournaise. PhD thesis, Université de La Réunion – OVPF/IPGP, Sainte-Clotilde, La Réunion, France, 500pp
- Bouidoire G, Brugier YA, Di Muro A, Wörner G, Arienzo I, Métrich N, Zanon V, Braukmüller N, Kronz A, Le Moigne Y, Michon L (2019) Eruptive activity on the western flank of Piton de la Fournaise (La Réunion Island, Indian Ocean): insights on magma transfer, storage and evolution at an oceanic volcanic island. *J Petrol* 60(9):1717–1752. <https://doi.org/10.1093/etrology/egz045>
- Bouidoire G, Liuzzo M, Di Muro A, Ferrazzini V, Michon L, Grassa F, Derrien A, Villeneuve N, Bourdeu A, Brunet C, Giudice G, Gurrieri S (2017) Investigating the deepest part of a volcano plumbing system: evidence for an active magma path below the western flank of Piton de la Fournaise (La Réunion Island). *J Volcanol Geoth Res* 341:193–207. <https://doi.org/10.1016/j.jvolgeores.2017.05.026>
- Bouidoire G, Rizzo AL, Arienzo I, Di Muro A (2020) Major contribution of a primitive mantle plume component in paroxysmal eruption of Piton de la Fournaise: inferences from helium isotopes. *Sci Rep* 10:1–16. <https://doi.org/10.1038/s41598-020-66260-x>
- Bouidoire G, Rizzo AL, Di Muro A, Grassa F, Liuzzo M (2018) Extensive CO₂ degassing in the upper mantle beneath oceanic basaltic volcanoes: first insights from Piton de la Fournaise volcano (La Réunion Island). *Geochim Cosmochim Acta* 235:376–401. <https://doi.org/10.1016/j.gca.2018.06.004>
- Bourdon B, Turner SP, Ribe NM (2005) Partial melting and upwelling rates beneath the Azores from a U-series isotope perspective. *Earth and Planetary Science Letters* 239(1–2):42–56. <https://doi.org/10.1016/j.epsl.2005.08.008>
- Brugier YA (2016) Magmatologie du Piton de la Fournaise (Ile de la Réunion) - Approche Volcanologique, Pétrologique et Expérimentale. Ph.D. thesis, Université d'Orléans, Orléans, France, 273pp
- Bucholz CE, Gaetani GA, Behn MD, Shimizu N (2013) Post-entrapment modification of volatiles and oxygen fugacity in olivine-hosted melt inclusions. *Earth Planet Sci Lett* 374:145–155. <https://doi.org/10.1016/j.epsl.2013.05.033>
- Bureau H, Métrich N, Pineau F, Semet M (1998a) Magma-conduit interaction at Piton de la Fournaise volcano (Réunion island): a melt and fluid inclusion study. *J Volcanol Geotherm Res* 84:39–60
- Bureau H, Métrich N, Semet MP, Staudacher T (1999) Fluid-magma decoupling in a hotspot volcano. *Geophys Res Lett* 26:3501
- Bureau H, Pineau F, Métrich N, Semet M, Javoy M (1998b) A melt and fluid inclusion study of the gas phase at Piton de la Fournaise volcano (Réunion island). *Chem Geol* 147:115–130
- Charvis P, Laesanpura A, Gallart J, Hirn A, Lepine J, de Voogd B, Minshull TA, Hello Y, Pontoise B (1999) Spatial distribution of hotspot material added to the lithosphere under La Réunion, from wide-angle seismic data. *J Geophys Res Solid Earth* 104(2):2875–2893. <https://doi.org/10.1029/98jb02841>
- Collins SJ, Pyle DM, MacLennan J (2009) Melt inclusions track pre-eruption storage and dehydration of magmas at Etna. *Geology* 37(6):571–574. <https://doi.org/10.1130/G30040A.1>
- Danyushevsky LV, Della-Pasqua FN, Sokolov S (2000) Re-equilibration of melt inclusions trapped by magnesian olivine phenocrysts from subduction-related magmas: petrological implications. *Contrib Mineral Petrol* 138:68–83. <https://doi.org/10.1007/PL00007664>
- Dasgupta R, Jackson MG, Lee CTA (2010) Major element chemistry of ocean island basalts - conditions of mantle melting and heterogeneity of mantle source. *Earth Planet Sci Lett* 289:377–392. <https://doi.org/10.1016/j.epsl.2009.11.027>
- Davis MG, Garcia MO, Wallace P (2003) Volatiles in glasses from Mauna Loa Volcano, Hawai'i: implications for magma degassing and contamination, and growth of Hawaiian volcanoes. *Contrib Mineral Petrol* 144:570–591. <https://doi.org/10.1007/s00410-002-0416-z>
- De Maesschalck R, Jouan-Rimbaud D, Massart DL (2000) The Mahalanobis distance. *Chemom Intell Lab Syst* 50:1–18. [https://doi.org/10.1016/S0169-7439\(99\)00047-7](https://doi.org/10.1016/S0169-7439(99)00047-7)
- Di Muro A, Métrich N, Allard P, Aiuppa A, Burton M, Galle B, Staudacher T (2016) Magma degassing at Piton de la Fournaise volcano. In: Bachèlery P, Lénat JF, Di Muro A, Michon L (ed) *Active volcanoes of the southwest Indian Ocean: Piton de la Fournaise and Karthala*. Active volcanoes of the world. Springer, Berlin, pp. 203–222
- Di Muro A, Métrich N, Vergani D, Rosi M, Armienti P, Fougereux T, Deloule E, Arienzo I, Civetta L (2014) The shallow plumbing system of Piton de la Fournaise volcano (La Réunion Island, Indian Ocean) revealed by the major 2007 caldera-forming eruption. *J Petrol* 55:1287–1315. <https://doi.org/10.1093/etrology/egu025>
- Di Muro A, Staudacher T, Ferrazzini V, Métrich M, Villemant B, Besson P, Garofalo C (2015) Shallow magma storage at Piton

- de la Fournaise Volcano after the 2007 summit caldera collapse tracked in Pele's hairs. In: Carey R, Cayol V, Poland M, Weis D (ed) *Hawaiian volcanoes: from source to surface*. Geophysical monograph series 208, pp. 189–212
- Duan X (2014) A general model for predicting the solubility behavior of H₂O–CO₂ fluids in silicate melts over a wide range of pressure, temperature and compositions. *Geochim Cosmochim Acta* 125:582–609. <https://doi.org/10.1016/j.gca.2013.10.018>
- Duan Z, Møller N, Weare JH (1992) Molecular dynamics simulation of PVT properties of geological fluids and a general equation of state of nonpolar and weakly polar gases up to 2000 K and 20,000 bar. *Geochim Cosmochim Acta* 56:3839–3845. [https://doi.org/10.1016/0016-7037\(92\)90175-1](https://doi.org/10.1016/0016-7037(92)90175-1)
- Duan Z, Møller N, Weare JH (1996) A general equation of state for supercritical fluid mixtures and molecular dynamics simulation of mixture PVTX properties. *Geochim Cosmochim Acta* 60:1209–1216. [https://doi.org/10.1016/0016-7037\(96\)00004-X](https://doi.org/10.1016/0016-7037(96)00004-X)
- Fall A, Tattitch B, Bodnar RJ (2011) Combined microthermometric and Raman spectroscopic technique to determine the salinity of H₂O–CO₂–NaCl fluid inclusions based on clathrate melting. *Geochim Cosmochim Acta* 75(4):951–964. <https://doi.org/10.1016/j.gca.2010.11.021>
- Famin V, Welsch B, Okumura S, Bachèlery P, Nakashima S (2009) Three differentiation stages of a single magma at Piton de la Fournaise volcano (Reunion hot spot). *Geochim Geophys Geosyst* 10(1). <https://doi.org/10.1029/2008gc002015>
- Fisk MR, Upton BGJ, Ford CE, White M (1988) Geochemical and experimental study of the genesis of magmas of Réunion island, Indian Ocean. *J Geophys Res* 93:4933–4950. <https://doi.org/10.1029/JB093iB05p04933>
- Fontaine FR, Barruol G, Tkalčić H, Wölbern I, Rumpker G, Bodin T, Haugmard M (2015) Crustal and uppermost mantle structure variation beneath La Réunion hotspot track. *Geophys J Int* 203:107–126. <https://doi.org/10.1093/gji/ggv279>
- Frezzotti ML, Tecce F, Casagli A (2012) Raman spectroscopy for fluid inclusion analysis. *J Geochem Explor* 112:1–20. <https://doi.org/10.1016/j.gexplo.2011.09.009>
- Gaetani GA, Watson EB (2002) Modelling the major-element evolution of olivine-hosted melt inclusions. *Chem Geol* 183:25–41. [https://doi.org/10.1016/S0009-2541\(01\)00370-9](https://doi.org/10.1016/S0009-2541(01)00370-9)
- Gallart J, Driad L, Charvis P, Sapin M, Hirn A, Diaz J, de Voogd B, Sachpazi M (1999) Perturbation to the lithosphere along the hotspot track of La Réunion from an offshore-onshore seismic transect. *J Geophys Res* 104:2895–2908. <https://doi.org/10.1029/98JB02840>
- Ghiorso MS, Hirschmann MM, Reiners PW, Kress VC (2001) The pMELTS: a revision of MELTS for improved calculation of phase relations and major element partitioning related to partial melting of the mantle to 3 GPa. *Geochim Geophys Geosyst* 3:1030. <https://doi.org/10.1029/2001GC000217>
- Ghiorso MS, Sack RO (1995) Chemical mass-transfer in magmatic processes IV. A Revised and Internally Consistent Thermodynamic Model for the Interpolation and Extrapolation of Liquid-Solid Equilibria in Magmatic Systems at Elevated-Temperatures and Pressures. *Contrib Miner Petrol* 119:197–212. <https://doi.org/10.1007/BF00307281>
- Gonnermann HM, Manga M (2005) Nonequilibrium magma degassing: results from modeling of the ca. 1340 AD eruption of Mono Craters, California. *Earth Planet Sci Lett* 238(1):1–16. <https://doi.org/10.1016/j.epsl.2005.07.021>
- Gurioli L, Di Muro A, Vlastélic I, Moune S, Thivet S, Valer M, Villeneuve N, Boudoire G, Peltier A, Bachèlery P, Ferrazzini V, Métrich N, Benbakkar M, Cluzel N, Constantin C, Devidal JL, Fonquernie C, Hénot JM (2018) Integrating field, textural, and geochemical monitoring to track eruption triggers and dynamics: a case study from Piton de la Fournaise. *Solid Earth* 9:431–455. <https://doi.org/10.5194/se-9-431-2018>
- Hagiwara Y, Yoshida K, Yoneda A, Torimoto J, Yamamoto J (2021) Experimental variable effects on laser heating of inclusions during Raman spectroscopic analysis. *Chem Geol* 559:119928. <https://doi.org/10.1016/j.chemgeo.2020.119928>
- Hammer JE, Jacob S, Welsch B, Hellebrand E, Sinton J (2016) Clinopyroxene in postshield Haleakala ankaramite. 1. Efficacy of thermobarometry. *Contrib Mineral Petrol* 171. <https://doi.org/10.1007/s00410-015-1212-x>
- Hansteen TH, Klügel A (2008) Fluid inclusion thermobarometry as a tracer for magmatic processes. *Rev Mineral Geochem* 69:143–177. <https://doi.org/10.2138/rmg.2008.69.5>
- Hanyu T, Dunai TJ, Davies GR, Kaneoka I, Nohda S, Uto K (2001) Noble gas study of the Réunion hot spot: evidence for distinct less-degassed mantle sources. *Earth Planet Sci Lett* 193:83–98. [https://doi.org/10.1016/S0012-821X\(01\)00489-7](https://doi.org/10.1016/S0012-821X(01)00489-7)
- Hanyu T, Yamamoto J, Kimoto K, Shimizu K, Ushikubo T (2020) Determination of total CO₂ in melt inclusions with shrinkage bubbles. *Chem Geol* 557:119855. <https://doi.org/10.1016/j.chemgeo.2020.119855>
- Hartley ME, Maclennan J, Edmonds M, Thordarson T (2014) Reconstructing the deep CO₂ degassing behaviour of large basaltic fissure eruptions. *Earth Planet Sci Lett* 393:120–131. <https://doi.org/10.1016/j.epsl.2014.02.031>
- Head E, Shaw AM, Wallace PJ, Sims KWW, Carn SA (2011) Insight into volatile behavior at Nyamuragira volcano (D.R. Congo, Africa) through olivine-hosted melt inclusions. *Geochim Geophys Geosyst* 12:Q0AB11. <https://doi.org/10.1029/2011GC003699>
- Hedenquist JW, Lowenstern JB (1994) The role of magmas in the formation of hydrothermal ore deposits. *Nature* 370:519–527. <https://doi.org/10.1038/370519a0>
- Helz RT, Clague DA, Sisson TW, Thornber CR (2014) Petrologic insights into basaltic volcanism at historically active Hawaiian volcanoes. In: Poland MP, Takahashi TJ, Landowski CM (ed) *Characteristics of Hawaiian Volcanoes*, pp. 237–292
- Helz RT, Thornber CR (1987) Geothermometry of Kilauea Iki lava lake, Hawaii. *Bull Volcanol* 49:651–668. <https://doi.org/10.1007/BF01080357>
- Hildner E, Klügel A, Hauff F (2011) Magma storage and ascent during the 1995 eruption of Fogo, Cape Verde Archipelago. *Contrib Miner Petrol* 162(4):751. <https://doi.org/10.1007/s00410-011-0623-6>
- Huang S, Frey FA, Blichert-Toft J, Fodor RV, Bauer GR, Xu G (2005) Enriched components in the Hawaiian plume: evidence from Kahooolawe Volcano, Hawaii. *Geochim Geophys Geosyst* 6(11). <https://doi.org/10.1029/2005GC001012>
- Jackson MG, Dasgupta R (2008) Compositions of HIMU, EM1, and EM2 from global trends between radiogenic isotopes and major elements in ocean island basalts. *Earth Planet Sci Lett* 276(1):175–186. <https://doi.org/10.1016/j.epsl.2008.09.023>
- Jenner FE, O'Neill HSC (2012) Major and trace analysis of basaltic glasses by laser-ablation ICP-MS. *Geochim Geophys Geosyst* 13:3. <https://doi.org/10.1029/2011GC003890>
- Jennings ES, Gibson SA, Maclennan J, Heinonen JS (2017) Deep mixing of mantle melts beneath continental flood basalt provinces: constraints from olivine-hosted melt inclusions in primitive magmas. *Geochim Cosmochim Acta* 196:36–57. <https://doi.org/10.1016/j.gca.2016.09.015>
- Johnson ER, Wallace PJ, Cashman KV, Granados HD (2010) Degassing of volatiles (H₂O, CO₂, S, Cl) during ascent, crystallization, and eruption at mafic monogenetic volcanoes in central Mexico. *J Volcanol Geotherm Res* 197:225–238. <https://doi.org/10.1016/j.jvolgeores.2010.02.017>

- Klügel A, Longpré MA, Garcia-Canada L, Stix J (2015) Deep intrusions, lateral magma transport and related uplift at ocean island volcanoes. *Earth and Planet Sci Lett* 431:140–149. <https://doi.org/10.1016/j.epsl.2015.09.031>
- Kobayashi T, Yamamoto J, Hirajima T, Ishibashi H, Hirano N, Lai Y, Prikhod'ko V, Arai S (2012) Conformity and precision of CO₂ densimetry in CO₂ inclusions: microthermometry versus Raman microspectroscopic densimetry. *J Raman Spectrosc* 43(8):1126–1133. <https://doi.org/10.1002/jrs.3134>
- Kouchi A, Sugawara Y, Kashima K, Sunagawa I (1983) Laboratory growth of sector zoned clinopyroxenes in the system CaMg-Si₂O₆-CaTiAl₂O₆. *Contrib Miner Petrol* 83:177–184. <https://doi.org/10.1007/BF00373091>
- Lamadrid HM, Moore LR, Moncada D, Rimstidt JD, Burruss RC, Bodnar RJ (2017) Reassessment of the Raman CO₂ densimeter. *Chem Geol*. <https://doi.org/10.1016/j.chemgeo.2016.12.034>
- Lange RA, Carmichael IS (1987) Densities of Na₂O-K₂O-CaO-MgO-FeO-Fe₂O₃-Al₂O₃-TiO₂-SiO₂ liquids: new measurements and derived partial molar properties. *Geochim Cosmochim Acta* 51(11):2931–2946. [https://doi.org/10.1016/0016-7037\(87\)90368-1](https://doi.org/10.1016/0016-7037(87)90368-1)
- Lénat JF, Bachèlery P, Merle O (2012) Anatomy of Piton de la Fournaise volcano (La Réunion, Indian Ocean). *Bull Volcanol* 74:1945–1961. <https://doi.org/10.1007/s00445-012-0640-y>
- Lenjoliné O, Duputel Z, Ferrazzini V (2016) Uncovering the hidden signature of a magmatic recharge at Piton de la Fournaise volcano using small earthquakes. *Geophys Res Lett* 43. <https://doi.org/10.1002/2016GL068383>
- Liuzzo M, Di Muro A, Giudice G, Michon L, Ferrazzini V, Gurrieri S (2015) New evidence of CO₂ soil degassing anomalies on Piton de la Fournaise volcano and the link with volcano tectonics structures. *Geochem Geophys Geosys* 16:4388–4404. <https://doi.org/10.1002/2015GC006032>
- Lowenstern JB (2001) Carbon dioxide in magmas and implications for hydrothermal systems. *Miner Deposita* 36:480–502. <https://doi.org/10.1007/s001260100185>
- Ludden JN (1978) Magmatic evolution of the basaltic shield volcanoes of Reunion Island. *J Volcanol Geoth Res* 4(1–2):171–198. [https://doi.org/10.1016/0377-0273\(78\)90035-5](https://doi.org/10.1016/0377-0273(78)90035-5)
- Maclennan J (2017) Bubble formation and decrepitation control the CO₂ content of olivine-hosted melt inclusions. *Geochem Geophys Geosyst* 18. <https://doi.org/10.1002/2016GC006633>
- Mahoney JJ, Duncan RA, Khan W, Gnos E, McCormick GR (2002) Cretaceous volcanic rocks of the South Tethyan suture zone, Pakistan: implications for the Réunion hotspot and Deccan Traps. *Earth Planet Sci Lett* 203:295–310. [https://doi.org/10.1016/S0012-821X\(02\)00840-3](https://doi.org/10.1016/S0012-821X(02)00840-3)
- Massare D, Métrich N, Clocchiatti R (2002) High-temperature experiments on silicate melt inclusions in olivine at 1 atm: inference on temperatures of homogenization and H₂O concentrations. *Chem Geol* 183:87–98
- Maurel C, Maurel P (1982) Etude expérimentale de l'équilibre Fe²⁺–Fe³⁺ dans les spinelles chromifères et les liquides silicatés basiques coexistant à 1 atm. *CR Acad Sci* 295:209–212
- Mercier M, Di Muro A, Giordano D, Métrich N, Lesne P, Pichavant M, Scaillet B, Clocchiatti R, Montagnac G (2009) Influence of glass polymerisation and oxidation on microRaman water analysis in aluminosilicate glasses. *Geochim Cosmochim Acta* 73:197–217. <https://doi.org/10.1016/j.gca.2008.09.030>
- Mercier M, Di Muro A, Métrich N, Giordano D, Belhadj O, Mandeville CW (2010) Spectroscopic analysis (FTIR, RAMAN) of water in mafic and intermediate glasses and glass inclusions. *Geochim Cosmochim Acta* 74:5641–5656. <https://doi.org/10.1016/j.gca.2010.06.020>
- Métrich N, Bertagnini A, Di Muro A (2010) Conditions of magma storage, degassing and ascent at Stromboli: new insights into the volcano plumbing system with inferences on the eruptive dynamics. *J Petrol* 51:603–626. <https://doi.org/10.1093/ptrology/egp083>
- Métrich N, Wallace PJ (2008) Volatile abundances in basaltic magmas and their degassing paths tracked by melt inclusions. *Minerals, Inclusions, and Volcanic Processes. Rev Mineral Geochem* 69:363–402. <https://doi.org/10.2138/rmg.2008.69.10>
- Métrich N, Zanon V, Créon L, Hildenbrand A, Moreira M, Marques FO (2014) Is the 'Azores hotspot' a wet spot? Insights from the geochemistry of fluid and melt inclusions in olivine of Pico basalts. *J Petrol* 55(2):377–393. <https://doi.org/10.1093/ptrology/egt071>
- Michon L, Ferrazzini V, Di Muro A, Villeneuve N, Famin V (2015) Rift zones and magma plumbing system of Piton de la Fournaise volcano: how do they differ from Hawaii and Etna. *J Volcanol Geotherm Res* 303:112–129. <https://doi.org/10.1016/j.jvolgeores.2015.07.031>
- Mollo S, Del Gaudio P, Ventura G, Iezzi G, Scarlato P (2010) Dependence of clinopyroxene composition on cooling rate in basaltic magmas: implications for thermobarometry. *Lithos* 118:302–312. <https://doi.org/10.1016/j.lithos.2010.05.006>
- Moore LR, Gazel E, Tuohy R, Lloyd AS, Esposito R, Steele-Macinnis M, Hauri ER, Wallace PJ, Plank T, Bodnar RJ (2015) Bubbles matter: an assessment of the contribution of vapor bubbles to melt inclusion budgets. *Am Mineral* 100(4):806–823. <https://doi.org/10.2138/am-2015-5036>
- Myers ML, Geist DJ, Rowe MC, Harpp KS, Wallace PJ, Dufek J (2014) Replenishment of volatile-rich mafic magma into a degassed chamber drives mixing and eruption of Tungurahua volcano. *Bull Volcanol* 76(11):872. <https://doi.org/10.1007/s00445-014-0872-0>
- Nauret F, Famin V, Vlastélic I, Gannoun A (2019) A trace of recycled continental crust in the Réunion hotspot. *Chem Geol* 524:67–76. <https://doi.org/10.1016/j.chemgeo.2019.06.009>
- Peltier A, Bachèlery P, Staudacher T (2009) Magma transport and storage at Piton de la Fournaise (La Réunion) between 1972 and 2007: A review of geophysical and geochemical data. *J Volcanol Geotherm Res* 184:93–108. <https://doi.org/10.1016/j.jvolgeores.2008.12.008>
- Peltier A, Poland M, Staudacher T (2015) Are Piton de la Fournaise (La Réunion) and Kīlauea (Hawai'i) really analog volcanoes? In: Carey R, Cayol V, Poland M, Weis D (ed) *Hawaiian Volcanoes: From Source to Surface*. John Wiley & Sons, Inc, (ch 23). <https://doi.org/10.1002/9781118872079>
- Peters BJ, Day JMD, Taylor LA (2016) Early mantle heterogeneities in the Réunion hotspot source inferred from highly siderophile elements in cumulate xenoliths. *Earth Planet Sci Lett* 448:150–160. <https://doi.org/10.1016/j.epsl.2016.05.015>
- Pichavant M, Brugier Y, Di Muro A (2016) Petrological and experimental constraints. In: Bachèlery P, Lénat JF, Di Muro A, Michon L (ed) *Active volcanoes of the southwest Indian Ocean: Piton de la Fournaise and Karthala*. Active volcanoes of the world. Springer, Berlin
- Pichavant M, Di Carlo I, Rotolo SG, Scaillet B, Burgisser A, Le Gall N, Martel C (2013) Generation of CO₂-rich melts during basalt magma ascent and degassing. *Contrib Miner Petrol* 166(2):545–561. <https://doi.org/10.1007/s00410-013-0890-5>
- Pietruszka AJ, Hauri EH, Blichert-Toft J (2009) Crustal contamination of mantle-derived magmas within Piton de la Fournaise volcano, Reunion island. *J Petrol* 50:661–684. <https://doi.org/10.1093/ptrology/egp016>
- Poland MP, Miklius A, Montgomery-Brown EK (2014) Magma supply, storage, and transport at shield-stage Hawaiian volcanoes. In Poland MP, Takahashi TJ, Landowski CM (ed) *Characteristics of Hawaiian Volcanoes*, U.S. Geol. Surv., pp. 179–234. <https://doi.org/10.3133/pp18015>

- Putirka KD (2008) Thermometers and barometers for volcanic systems. *Rev Mineral Geochem* 69:61–120. <https://doi.org/10.2138/rmg.2008.69.3>
- Quidelleur X, Holt JW, Salvany T, Bouquerel H (2010) The double structure of the Réunion geomagnetic event based on new K-Ar ages from the type locality, massif de la Montagne, Réunion Island (Indian Ocean) and assessment of the global context. *Geophys J Int* 182:699–710
- Rae AS, Edmonds M, MacLennan J, Morgan D, Houghton B, Hartley ME, Sides I (2016) Time scales of magma transport and mixing at Kīlauea Volcano, Hawai'i. *Geology* 44(6):463–466. <https://doi.org/10.1130/G37800.1>
- Reiners PW, Nelson BK (1998) Temporal-compositional-isotopic trends in rejuvenated-stage magmas of Kauai, Hawaii, and implications for mantle melting processes. *Geochim Cosmochim Acta* 62(13):2347–2368. [https://doi.org/10.1016/S0016-7037\(98\)00141-0](https://doi.org/10.1016/S0016-7037(98)00141-0)
- Rhodes JM (1996) Geochemical stratigraphy of lava flows sampled by the Hawaii Scientific Drilling Project. *J Geophys Res* 101:11729. <https://doi.org/10.1029/95JB03704>
- Riker J (2005) The 1859 Eruption of Mauna Loa Volcano, Hawai'i: controls on the development of long lava channels. Master's thesis, University of Oregon, pp. 117–127
- Roult G, Peltier A, Taisne B, Staudacher T, Ferrazzini V, Di Muro A (2012) A new comprehensive classification of the Piton de la Fournaise activity spanning the 1985–2010 period. Search and analysis of short-term precursors from a broad-band seismological station. *Journal of Volcanology and Geothermal Research* 241:78–104. <https://doi.org/10.1016/j.jvolgeores.2012.06.012>
- Salters VJ, Stracke A (2004) Composition of the depleted mantle. *Geochem Geophys Geosyst* 5(5). <https://doi.org/10.1029/2003GC000597>
- Salvany T, Lahitte P, Nativel P, Gillot PY (2012) Geomorphic evolution of the Piton des Neiges volcano (Réunion Island, Indian Ocean): competition between volcanic construction and erosion since 1.4 Ma. *Geomorphology* 136:132–147. <https://doi.org/10.1016/j.geomorph.2011.06.009>
- Schipper CI, Jakobsson SP, White JDL, Palin JM, Bush-Marcinowski T (2015) The Surtsey magma series. *Sci Rep* 5:11498. <https://doi.org/10.1038/srep11498>
- Schipper CI, Le Voyer M, Moussallam Y, White JDL, Thordarson T, Kimura JI, Chang Q (2016) Degassing and magma mixing during the eruption of Surtsey Volcano (Iceland, 1963–1967): the signatures of a dynamic and discrete rift propagation event. *Bull Volcanol* 78. <https://doi.org/10.1007/s00445-016-1025-4>
- Smietana M (2011) Pétrologie, géochronologie (K–Ar) et géochimie élémentaire et isotopique (Sr, Nd, Hf, Pb) des laves anciennes de La Réunion. Implications sur la construction de l'édifice volcanique. PhD thesis, Université de La Réunion, Sainte-Clotilde, France, 362pp
- Sobolev AV, Chaussidon M (1996) H₂O concentrations in primary melts from supra-subduction zones and mid-ocean ridges: implications for H₂O storage and recycling in the mantle. *Earth Planet Sci Lett* 137(1–4):45–55. [https://doi.org/10.1016/0012-821X\(95\)00203-O](https://doi.org/10.1016/0012-821X(95)00203-O)
- Song Y, Chou IM, Hu W, Robert B, Lu W (2009) CO₂ density-Raman shift relation derived from synthetic inclusions in fused silica capillaries and its application. *Acta Geol Sin* 83(5):932–938
- Spilliaert N, Allard P, Métrich N, Sobolev A (2006) Melt inclusion record of the conditions of ascent, degassing and extrusion of volatile-rich alkali basalt during the powerful 2002 flank eruption of Mount Etna (Italy). *J Geophys Res* 111:B04203. <https://doi.org/10.1029/2005/JB003934>
- Tuohy RM, Wallace PJ, Loewen MW, Swanson DA, Kent AJR (2016) Magma transport and olivine crystallization depths in Kīlauea's east rift zone inferred from experimentally rehomogenized melt inclusions. *Geochim Cosmochim Acta* 185:232–250. <https://doi.org/10.1016/j.gca.2016.04.020>
- Upton BGI, Semet M, Joron JL (2000) Cumulate clasts in the Bellecombe Ash Member, Piton de la Fournaise, Réunion Island, and their bearing on cumulative processes in the petrogenesis of the Réunion lavas. *J Volcanol Geotherm Res* 104:297–318. [https://doi.org/10.1016/S0377-0273\(00\)00212-2](https://doi.org/10.1016/S0377-0273(00)00212-2)
- Upton BGI, Wadsworth WJ (1966) The basalts of Réunion island, Indian Ocean. *Bull Volcanol* 29:7–23. <https://doi.org/10.1007/BF02597136>
- Valer M (2016) Caractérisation des stockages magmatiques profonds sous les volcans de La Réunion: apports de la pétro-géochimie des inclusions magmatiques. PhD thesis, Université Clermont Auvergne, Clermont-Ferrand, France
- Valer M, Schiano P, Bachèlery P (2017) Geochemical characteristics of La Réunion mantle plume source inferred from olivine-hosted melt inclusions from the adventive cones of Piton de la Fournaise volcano (La Réunion Island). *Contribution. Mineral. Petrol.* 172:74. <https://doi.org/10.1007/s00410-017-1397-2>
- van den Kerkhof AM, Olsen SN (1990) A natural example of superdense CO₂ inclusions: microthermometry and Raman analysis. *Geochim Cosmochim Acta* 55:2533–2544
- Venugopal S, Schiavi F, Moune S, Bolfan-Casanova N, Druitt T, Williams-Jones G (2020) Melt inclusion vapour bubbles: the hidden reservoir for major and volatile elements. *Sci Rep* 10(1):1–14. <https://doi.org/10.1038/s41598-020-65226-3>
- Vigouroux N, Williams-Jones AE, Wallace P, Staudacher T (2009) The November 2002 eruption of Piton de la Fournaise, Réunion: tracking the pre-eruptive thermal evolution of magma using melt inclusions. *Bull Volcanol* 71:1077–1089. <https://doi.org/10.1007/s00445-009-0287-5>
- Villemant B, Salaün A, Staudacher T (2009) Evidence for a homogeneous primary magma at Piton de la Fournaise (La Réunion): a geochemical study of matrix glass, melt inclusions and Pélé's hairs of the 1998–2008 eruptive activity. *J Volcanol Geoth Res* 184:79–92. <https://doi.org/10.1016/j.jvolgeores.2009.03.015>
- Villeneuve N, Bachèlery P (2006) Revue de la typologie des éruptions au Piton de la Fournaise, processus et risques volcaniques associés. *CyberGeo*. <https://doi.org/10.4000/cyberge.2536> (<http://cyberge.revues.org/2536>)
- Vlastélic I, Di Muro A, Bachèlery P, Gurioli L, Auclair D, Gannoun A (2018) Control of source fertility on the eruptive activity of Piton de la Fournaise volcano, La Réunion. *Sci Rep* 8:14478. <https://doi.org/10.1038/s41598-018-32809-0>
- Vlastélic I, Staudacher T, Bachèlery P, Télouk P, Neuville D, Benbakkar M (2011) Lithium isotope fractionation during magma degassing: constraints from silicic differentiates and natural gas condensates from Piton de la Fournaise. *Chem Geol* 284:26–34. <https://doi.org/10.1016/j.chemgeo.2011.02.002>
- Wallace PJ, Kamenetsky VS, Cervantes P (2015) Melt inclusion CO₂ contents, pressures of olivine crystallization, and the problem of shrinkage bubbles. *Am Mineral* 100(4):787–794. <https://doi.org/10.2138/am-2015-5029>
- Walther G, Frese I, Di Muro A, Kueppers U, Michon L, Métrich N (2015) The eruptive history of the Troux Blancs pit craters, La Réunion Island: the origin of a 24 km long lava flow. *EGU General Assembly 2015*
- Wang HS, Lineweaver CH, Ireland TR (2018) The elemental abundances (with uncertainties) of the most Earth-like planet. *Icarus* 299:460–474. <https://doi.org/10.1016/j.icarus.2017.08.024>
- Wang X, Chou IM, Hu W, Burruss RC, Sun Q, Song Y (2011) Raman spectroscopic measurements of CO₂ density: experimental calibration with high-pressure optical cell (HPOC) and fused

- silica capillary capsule (FSCC) with application to fluid inclusion observations. *Geochim Cosmochim Acta* 75(14):4080–4093. <https://doi.org/10.1016/j.gca.2011.04.028>
- Welsch B, Famin V, Baronnet A, Bachèlery P (2013) Dendritic crystallization: a single process for all textures of olivine in basalts? *J Petrol* 54:539–574. <https://doi.org/10.1093/petrology/egs077>
- Welsch B, Faure F, Bachèlery P, Famin V (2009) Microcrysts record transient convection at Piton de la Fournaise Volcano (La Réunion hotspot). *J Petrol* 50:2287–2305. <https://doi.org/10.1093/petrology/egp076>
- Witham F (2011) Conduit convection, magma mixing, and melt inclusion trends at persistent degassing volcanoes. *Earth Planet Sci Lett* 301:345–352. <https://doi.org/10.1016/j.epsl.2010.11.017>
- Workman RK, Hart SR (2005) Major and trace element composition of the depleted MORB mantle (DMM). *Earth Planet Sci Lett* 231:53–72. <https://doi.org/10.1016/j.epsl.2004.12.005>
- Yoshimura S (2015) Diffusive fractionation of H₂O and CO₂ during magma degassing. *Chem Geol* 411:172–181. <https://doi.org/10.1016/j.chemgeo.2015.07.003>